

THE PENNSYLVANIA STATE UNIVERSITY
SCHREYER HONORS COLLEGE

DEPARTMENT OF BIOMEDICAL ENGINEERING

Localized Thrombus Rheology: A Study through the Development of a Magnetic Bead
Microrheometry System

PRITHVI NILKANT
SPRING 2015

A thesis
submitted in partial fulfillment
of the requirements
for baccalaureate degrees
in Mechanical Engineering and Biomedical Engineering
with honors in Biomedical Engineering

Reviewed and approved* by the following:

Keefe Manning
Associate Professor of Biomedical Engineering and Surgery
Thesis Supervisor and Honors Advisor

Peter Butler
Professor of Biomedical Engineering
Faculty Reader

* Signatures are on file in the Schreyer Honors College.

ABSTRACT

Cardiovascular disease (CVD) has manifested into a significant public health epidemic over the last thirty years. Atherosclerosis, the most common cause of CVD death, and implantable devices, designed to treat numerous issues resulting from CVD, impact hemodynamics. Consequently, both scenarios increase the likelihood of triggering the coagulation cascade, leading to thrombus formation, and the potential for thromboembolism. Thromboembolism is the breakage and subsequent circulation of a blood clot through the body due to shear stresses induced by blood flow. It substantially increases the risk of many serious medical conditions such as heart attacks or strokes. Studying the elasticity of thrombi can give researchers insight into growth patterns, locations where it is strongest and weakest, and the mechanisms of thromboembolism, which are all imperative when considering the development of preventative treatments and measures. Because thrombi are very heterogeneous materials, it is important to study the elasticity on a local level. The chief objective of this study is to develop and optimize a microrheometry system to test and measure the mechanical properties of thrombi, specifically elasticity. The force from an external magnet was calculated at various points throughout the working range of the experimental system using viscous glycerol-albumin solution samples with embedded fluorescent paramagnetic beads. The displacement of these beads in response to the magnetic force were imaged and tracked over time; Stoke's law was then used to calculate the drag force on the beads induced by the bar magnet at each position. It was seen that the force from this bar magnet is on the order of piconewtons, and an equation for this force as a function of distance away from the magnet was empirically derived. Preliminary experiments of thrombi of unknown elasticity have been tested. Initial results using our setup show rough elastic displacement responses; thus, there is confidence that in the future, this developed microrheometry system can be used and further refined to measure local elasticities of thrombi.

TABLE OF CONTENTS

List of Figures	iii
List of Tables	iv
Acknowledgements.....	v
Chapter 1 Introduction	1
Fluid Dynamics	2
The Coagulation Cascade	3
Thromboembolism.....	5
Clot Rheology	6
Magnetic Bead Microrheology	7
Chapter 2 Methods.....	9
Preparation of Substrate and Polyacrylamide Hydrogel Formation	10
Experimental Setup with Magnet and Imaging Process	13
Experimental Testing of Polyacrylamide Hydrogels	15
Determination of Bead Position.....	17
Data Analysis, Testing, and Optimization of Experimental Setup	19
Drag Force	25
Faxen's Law.....	27
Experimentation with Viscous Fluid	29
Bovine Blood Preparation and Thrombus Formation	29
Chapter 3 Results	31
Bar Magnet Testing in Viscous Fluid	31
Fitting Data to Theoretical Model Equation	51
Deformation of Beads in Bovine Thrombi	53
Chapter 4 Discussion	62
Polyacrylamide Hydrogel Testing with Electromagnet	62
Viscous Fluid Testing with Bar Magnet	63
Force Calculations and Empirically Derived Equation.....	64
Experimentation on Bovine Blood Thrombi.....	65
Conclusions and Future Work	68
BIBLIOGRAPHY	70
Appendix A Solidworks Drawing of Sample and Magnet Holder	73
ACADEMIC VITA.....	75

LIST OF FIGURES

Figure 1: ⁷ A stenotic vessel.	3
Figure 2: ¹⁴ The coagulation cascade.	5
Figure 3: Electromagnet and hydrogel sample held by fixture and clamp on microscope stage and connected to power supply.	14
Figure 4: Electromagnet control setup.	15
Figure 5: Bar magnet and hydrogel sample held by fixture and clamp on microscope stage.	15
Figure 6: Corner of microscope slide defined as origin of entire system.	17
Figure 7: Diagram of the system with dimensions showing the working range of the system relative to the bar magnet.	18
Figure 8: Image of one position with three beads in the frame.	19
Figure 9: Common displacement traces of beads in a hydrogel during a trial.	20
Figure 10: Modification to the fixture to raise the hydrogel sample to rest in line with the center of the electromagnet.	21
Figure 11: Fabricated motor-device for rotation of the sample.	22
Figure 12: Image of magnetic beads embedded in hydrogel.	23
Figure 13: Locations where temperatures were measured in the system.	24
Figure 14: Faxen's Law.	28
Figure 15: Prepared bovine thrombus sample.	30
Figure 16: Representative displacement data of one trial at one position containing four beads in the image.	37
Figure 17: Velocities at various positions within the working range of system.	38
Figure 18: Force Distribution of Bar Magnet.	51
Figure 19: Theoretical magnetic field strength decay of a bar magnet with dimensions of 0.25 in x 0.25 in x 1 in as distance away from the magnet increases.	52
Figure 20: Experimental force data overlaid by the theoretical curve outputted by the curve-fitting software.	53

Figure 21: Common Displacement Response Shape in Bovine Thrombus. Displacement of a bead within a bovine thrombus sample.	54
Figure 22: Spring Constant vs Position in Blood Clot.	59
Figure 23: Characteristic bead displacement responses in three different mediums: Top plot (Whole Bovine Blood), middle plot (Platelet-Rich Plasma and White Buffy Coat Solution), and bottom plot (Packed Red Blood Cells).	60
Figure 24: Bright-field Microscopy of each sample from left to right.	61

LIST OF TABLES

Table 1: ²⁵ Four different concentrations of stock solutions used to make polyacrylamide hydrogels of varying elasticities.	12
Table 2: Temperature increase at various points in the system.	25
Table 3: Locations of beads in fluid with viscosity of 2.1 cP relative to origin	33
Table 4: Velocity values and calculated magnetic force acting on beads immersed in a 2.1 cP viscosity fluid at specific positions.....	39
Table 5: Velocity values and calculated magnetic force acting on beads immersed in a 12 cP viscosity fluid at specific positions.....	43
Table 6: Summary of data for three bovine thrombi tested.	56

ACKNOWLEDGEMENTS

I would like to thank Andrew Rogers for mentoring me as a sophomore student, while this project was his own. He taught me the theory, procedures, and data analysis, and left me prepared to take over the project and succeed. I would also like to thank Gene Gerber and Gary Meyers for their manufacturing skills and technical assistance. Their accessibility and willingness to help were instrumental in moving this project forward. I would also like to thank two undergraduate researchers, Kristen Hagenah and Maya Janakowski, who aided me tremendously in helping to run experiments and process the enormous amount of data collected.

I would especially like to thank both Dr. Butler and Dr. Manning for the opportunity and resources they provided. Thank you to Dr. Manning for accepting me to the Artificial Heart Lab and providing me this research opportunity and to Dr. Butler for trusting me with the use of his laboratory and expensive equipment. Throughout this process, they provided invaluable advice, guidance, and expertise on a variety of engineering principles to teach me and push the project further.

Lastly, I would like to thank my parents and sister for their continual support throughout my life and my education. This would not have been possible without the motivation, discipline, and character I have learned from them.

Chapter 1

Introduction

The increasing prevalence of cardiovascular disease over the last thirty years has made it a significant public health epidemic. Cardiovascular disease encompasses a number of conditions that affect the function of the heart and blood vessels such as coronary artery disease, heart valve disease, and vascular disease. It is the leading cause of death worldwide, and accounts for over 33 percent of deaths in the United States.¹ Hereditary factors such as hypertension combined with lifestyle factors that are more prevalent than decades ago such as physical inactivity, unhealthy diet, obesity, and smoking increase the risk of developing this disease significantly. In 2006, healthcare expenditures related to cardiovascular disease exceeded 400 billion dollars, an astounding figure that shows a need for extensive research into this area.¹

Atherosclerosis is the hardening and narrowing of the vasculature lumen; it causes many deaths from heart attack and stroke and accounts for nearly three-fourths of all deaths from cardiovascular disease.² The process of atherosclerosis is triggered by local oxidation of lipoproteins, endothelial injury from fluid dynamics, or presence of toxins.³ Monocytes aggregate to the area of injury and penetrate the intima as lipids accumulate, engulfing lipids in the process. This process of the formation of foam cells overtime leads to the development of a fatty streak. As smooth muscle cells also migrate to the area, the lesion eventually develops into plaque.³ Although advanced lesions can grow sufficiently large to block blood flow, the most important clinical complication is an acute occlusion due to the formation of a thrombus or blood clot.⁴ The most common areas for atherosclerosis to develop include regions of branching, bifurcating, and

curvature, due to an increased likelihood of flow separation. The consequences of atherosclerosis can be seen in the disruption and alteration of the flow of blood through the body.

Fluid Dynamics

A combination of physiological factors and fundamental fluid dynamics principles are key factors in the detrimental effects related to atherosclerosis. A common occurrence in vessels exhibiting atherosclerosis is the creation of a stenosis, a narrowing of the vessel lumen due to a lesion, and the resulting unusual hemodynamic conditions may cause an abnormal biological response.⁵ Blood flow is forced to increase in speed moving through a stenosis due to the reduction in cross-sectional area, creating a high velocity jet.⁶ Downstream of the stenosis, the area then increases, and this rapid change of velocity and pressure, explained through the principles of the Bernoulli equation, can lead to flow separation and recirculation, exhibited in Figure 1. Continuity of flow describes this inverse relationship between cross-sectional area of a flow path and flow velocity; because the mass of a moving fluid does not change as it flows, the volume flow rate has the same value at all points along a tube.⁶ Recirculation of blood in a region is likely to cause thrombus formation and growth.

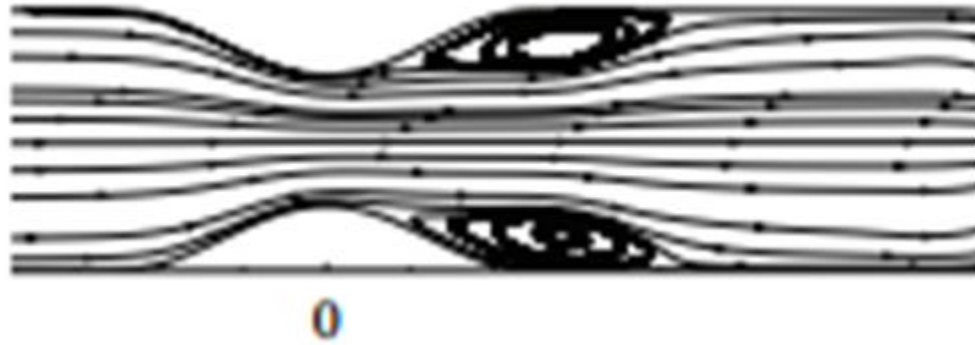


Figure 1:⁷ A stenotic vessel. The characteristic circular flow pattern exhibited just after the expansion in diameter of the vessel represents separation of flow. It is in this region where the risk of thrombus formation and growth is high.

Aside from pathological conditions, patients with implantable devices also face significant risk of thrombus formation. Devices such as prosthetic valves, ventricular assist devices, and artificial hearts, no matter the design, all alter the flow of blood through the cardiovascular system in some way. Specifically, thromboembolism is one of the main concerns in patients with ventricular assist devices, with a reported incidence of thromboembolic events ranging from 10% to 25%.⁸ In addition, the introduction of foreign material to the body induces adverse reactions with blood. The hemocompatibility of the biomaterial used in an implantable device has been observed clinically to be as significant as prolonged activation of endothelial and coagulation systems after implantation of ventricular assist devices.⁹ Activated blood coagulation is an essential determinant of the risk of atherothrombotic complications.¹⁰ As such, the interaction of blood with foreign materials and thrombosis in general is explained through a description of the coagulation cascade.

The Coagulation Cascade

Coagulation involves the regulated sequence of proteolytic activation of a series of zymogens to achieve appropriate and timely hemostasis in an injured vessel.¹¹ The blood

coagulation system comprises three basic elements: platelet adhesion, activation, and aggregation, fibrin formation, and fibrinolysis.¹⁰ Under pathophysiological conditions, blood coagulation is activated along the principles of Virchow's triad, which indicate that thrombosis always occurs through the interaction of three components: an altered vessel wall, an impaired or changed pattern of blood flow, and an altered blood composition.¹⁰

The cascade process, shown in Figure 2, can follow two different beginning pathways, intrinsic or extrinsic, that both lead to the same final pathway of thrombus formation. The extrinsic process is triggered by vessel injury; endothelial cells and platelets activate, due to exposed tissue thromboplastin (tissue factor), and aggregate to the site. The activation of platelets induces the release of von Willebrand factor, a protein that under high shear conditions binds to platelet membrane glycoproteins and exposed endothelial connective tissue to support the adhesion of platelets at the site of injury.¹² The platelet release reaction is also associated with the secretion of different metabolites contained in the intraplatelet organelles such as serotonin, calcium ions, and adenosine diphosphate.^{12,13} The result of platelet-endothelial aggregation yields a secure basis for fibrin formation. The tissue factor released during injury is a type of transmembrane glycoprotein with a strong affinity for Factor VII, activating it and enhancing its catalytic activity, in order for the complex to activate Factor X.¹² The intrinsic pathway, conversely, is triggered by surface mediation. When blood comes into contact with negatively charged surfaces, a series of proteolytic reactions are initiated that result in the activation of the plasma proteases Factor XII, kallikrein, Factor XI, and the cleavage of high molecular weight kininogen.¹⁴ A cascade of activations is thus triggered, with Factor XII activating Factor XI, IX, and XIII, and finally Factor X.¹⁴ With the activation of Factor X, the common pathway, shared by both the initial intrinsic and extrinsic pathways, begins. The combination of Factor X and V, and calcium ions catalyze the reaction of prothrombin to thrombin.¹² The production of thrombin initiates even further activation of platelets, thus amplifying the entire process. Furthermore,

thrombin activates Factor XIII and catalyzes the conversion of fibrinogen to unstable fibrin.¹² The unstable fibrin and Factor XIII combine to form a stable fibrin polymer that creates the mesh network of a stable blood clot.

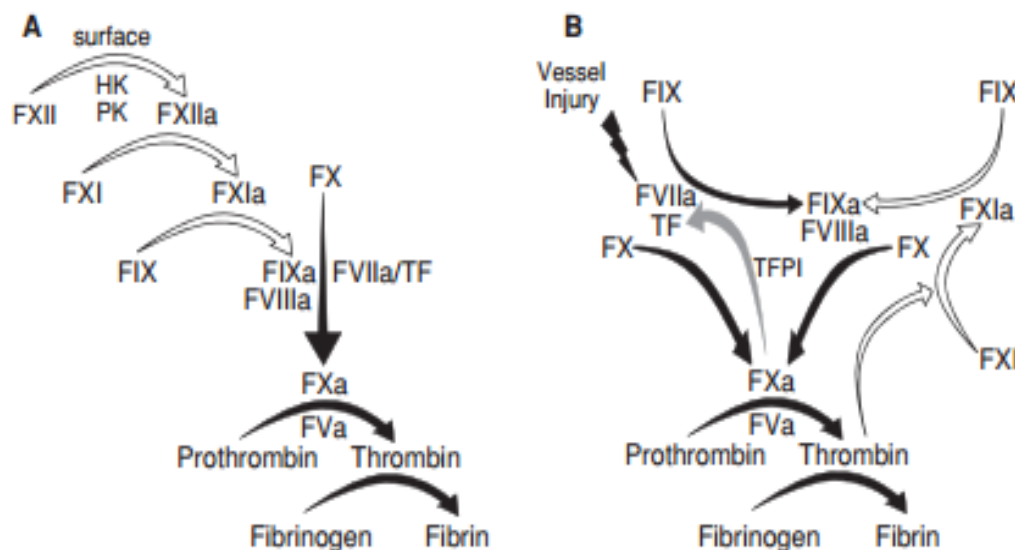


Figure 2:¹⁴ The coagulation cascade. Diagram A illustrates the intrinsic pathway. A negatively-charged surface leads to activation of Factor VII, and in turn activation of Factors XI, IX, VII, and X follows. Diagram B illustrates the extrinsic pathway. Vessel injury and the exposure of collagen lead to activation of Factor VII, and subsequent activation of Factor X. Factor X forms a complex with activated Factor V to convert prothrombin to thrombin. Lastly, thrombin activates fibrinogen to fibrin, resulting in a stable mesh network for thrombus formation.

Thromboembolism

The risk of occluding blood flow is high in the instance of formation of blood clots in the cardiovascular system. The most probable cause of such an occlusion is thromboembolism, the breaking of a thrombus and its subsequent circulation throughout the cardiovascular system.

Heart attack and stroke are common byproducts of thromboembolism, due to the emboli becoming lodged in a small vessel; in fact, the incidence of venous thromboembolic events is nearly identical to the incidence rates for stroke and fatal/nonfatal myocardial infarction.¹⁵ Due to variations in the composition of the thrombus, its geometry, and the surrounding flow field, the

analysis of thromboembolism is quite complex. A thrombus, just as any other material, will deform and embolize based on properties of strength and elasticity. Studying the mechanical properties of blood clots can yield valuable insight into the growth pattern of thrombi and thromboembolism, in order to develop preventative treatments and measures.

Clot Rheology

Thromboembolism occurs due to stresses deforming the material to the point of fracture and separation. Thus, it is important to use techniques of rheology to better understand this phenomenon. Rheology is the study of the deformation and flow of a material in response to applied stress.¹⁶ The applied stress, in the case of thromboembolism, is the shear stresses from blood flow over the growing thrombus. Analysis and study of the mechanical response of thrombi to shear stresses from blood flow are needed to develop a greater understanding of clot development and embolism.

The development of thrombi is very much dependent on the flow field and fluid dynamics that it is subjected to, as described in depth previously. To accurately study thrombi *in vitro* and draw links to *in vivo*, the process of coagulation as it pertains to fluid dynamics physiologically must be properly simulated so that the clot composition is realistic. This can be done using a bench top blood flow loop and a backward-facing step geometry model. An issue with previous studies of clot rheology is their method of coagulation; previous studies simply let blood coagulate in a tube or dish, with mild orbital swirling or a completely still environment, until adequate gelation occurred.^{17–19} This method of simulating *in vivo* coagulation is a poor representation of physiological thrombogenesis because it has no representation of flow field factors that affect clot composition. Thus, thrombi developed using such methods are unlikely to

possess the same cross-linked mesh and properties that a clot formed *in vivo* would naturally exhibit.

Also, as reflected in the discussion of the complex nature of the coagulation cascade, thrombi are very heterogeneous materials. Clot stiffness is thought to be strongly dependent on fibrin fiber thickness and flexural stiffness, branchpoint density, and fibrin concentration, though quantitative correlations between the structural features of clots and their rheology have not been made due to the difficulty of analyzing the morphology of the complex fibrin networks.¹⁷ Covalent cross-linking within fibrin networks produces dramatic effects on clot rheological properties.¹⁷ However, previous work done in this area has not taken this into account, instead assuming a more homogenous material.¹⁷⁻¹⁹ These experiments used cone and plate rheometers, which can only provide an average value of the deformation, and do not allow for local measurements in inhomogeneous systems.^{16,20} Because of the complexity and number of factors that affect the development and composition of thrombi, an average measurement is of little use in identifying correlations between local composition and local elasticity. To address these issues, a new class of microrheology techniques has emerged, to probe the material response on micrometer length scales with microliter sample volumes.¹⁶ Microrheology methods typically use embedded micron-size probes to locally deform a sample, and may involve active manipulation of the probes by local application of stress or by measuring passive motions of particles due to thermal fluctuations.¹⁶

Magnetic Bead Microrheology

This study used magnetic bead microrheology, which is based on the evaluation of magnetically driven local motion of paramagnetic beads of micron-scale embedded in the mesh-network and analyzed with fast image processing techniques.²⁰ In previous studies, magnetic bead

microrheology has been used to study elastic and viscoelastic properties of cytoskeletal filaments and actin networks.²⁰⁻²² When constructing a magnetic bead microrheometry system, thought must be given to the amount of force the particles should be subjected to as factors such as particle size, magnet size, and distance all contribute. In the past, a magnetic bead microrheometer was designed to achieve forces up to 10^4 pico-Newtons.²¹ The advantage of this type of experimental setup is that it can be built at low cost and operated without specialized optics expertise, enabling its broad use in a variety of biomedical research areas.²¹ Also, previous setups have typically required microscope modifications and additional instrumentation in order to manipulate the magnetic field and apply force.²¹ The motion of the paramagnetic beads is generated through a magnetic force field, and the material is thus subjected to a load to resist the movement of the beads.

The purpose of this study is to develop and optimize a repeatable magnetic bead microrheometry system to test and measure the mechanical properties, specifically elasticity, of thrombi formed through a bench top flow loop and backward-facing step model. Data of applied force and displacement was obtained using an external magnet and particle tracking methods, which were related to stresses and strains. From there, Hooke's Law was used to calculate localized elasticities to predict areas of the thrombus at risk of embolism.

Chapter 2

Methods

Thrombi are strained or deformed due to the shear stresses of blood flow. This relationship between stress (σ) and strain (ε) can be quantified by the application of Hooke's Law (Equation 1) to yield a value of elasticity (E).

$$\sigma = E * \varepsilon \quad (\text{Equation 1})$$

Because the purpose of this study is to determine the elasticity of thrombi, stress and strain data must be obtained. Stress will be induced through forces generated from a magnetic field, while the resulting strain will be measured by tracking the displacement of the paramagnetic beads embedded in the sample with a fluorescent microscope and imaging and tracking software. However, the force from the magnet which induces stress on the sample is not a property of the magnet that is readily known. Because the magnetic field generated from a bar magnet or electromagnet changes based on a bead's position relative to the magnet, an experiment must first be conducted to determine the strength of the magnetic field at various points throughout the system. This is done by using magnetic bead microrheology on a material of known elasticity. In this way, a strain can be measured through particle tracking, and since the elasticity is predetermined for the sample material, the stress, and thus the magnetic force at that location, can be calculated. Doing this repeatedly across the entire working area of the experimental setup will yield values of the magnetic force at various locations. A map of the magnitude of the magnetic field can then be created to calibrate the entire working range of the experimental setup. It is then possible to apply this magnetic field to a sample of unknown elasticity.

Preparation of Substrate and Polyacrylamide Hydrogel Formation

Polyacrylamide hydrogels were the substance of known elasticity used to determine the force of the magnetic field. Chemically cross-linked polyacrylamide is a polymeric gel that forms via the free-radical polymerization of acrylamide monomers after the addition of bis-acrylamide.²³ The extent of reaction is directly proportional to the amount of bis-acrylamide; therefore, equilibrated samples can be prepared at various points during the gelation process by varying the concentration of bis-acrylamide.²³ Thus, these gels have an easily tunable elasticity, along with being clear, and deforming and recovering linearly and rapidly. Polyacrylamide hydrogels have been used in the past to simulate and study the extracellular matrix, various biomaterials, and collagen, by measuring traction forces and the deformation of the gel based on Hooke's law from elasticity theory.²⁴⁻²⁶ Polyacrylamide is a popular medium for examining the response to the stiffness of a surrounding environment of biomedical applications because of its experimentally tested biocompatibility and tunable mechanical properties.²⁴ These gels have the ability to be prepared with identical mechanical properties of soft tissues.²⁴

The protocol for making these gels was obtained and conducted similarly to an investigation using hydrogels to study the extracellular matrix.²⁵ Coverslips and glass microscope slides first underwent surface activation to ensure complete binding of the gel. The coverslips (18 mm x 18 mm, VWR, Radnor, Pennsylvania) and slides (3'' x 1'' x 1mm, Fisher Scientific, Pittsburgh, Pennsylvania) were first passed through the flame of a Bunsen burner, dipped into 0.1 N NaOH (VWR), and then allowed to air dry. Next, full strength 3-aminopropyltrimethoxysilane (Sigma-Aldrich, St. Louis, Missouri) was diluted in isopropanol (Sigma-Aldrich) to a final concentration of 2% (1 mL 3-aminopropyltrimethoxysilane, 49 mL isopropanol) in a glass dish. Coverslips and slides were immersed in this solution for ten minutes inside the fume hood while gently stirring by hand. After washing the coverslips and slides in double distilled water (ddH₂O) through four exchanges of water at five minutes per exchange, they were immersed in 1%

glutaraldehyde (VWR) solution (2 mL glutaraldehyde, 48 mL ddH₂O) for thirty minutes, again stirring by hand in the fume hood. Finally, the coverslips and slides were washed by three exchanges of ddH₂O for five minutes per exchange with stirring and left to dry at room temperature in a container covered with aluminum foil to prevent dust from settling on the surfaces.

Stock solutions of acrylamide/bis-acrylamide mix from 40% acrylamide (VWR) and 2% bis-acrylamide (VWR) were prepared following the concentrations shown in Table 1 to the desired Modulus of Elasticity.²⁵ The values of hydrogel elasticity shown in Table 1 were chosen based on the elasticity of blood clots found in previous research studies.²⁵ It is important to note that in order to achieve 0.1% weight by volume for the ratio of beads to solution volume, a portion of volume of water was not added initially and was made up during the addition of the beads to the solution. The magnetic beads were provided in a solution of water. A concentration of 0.1% w/v was chosen so that when conducting experimentation with a hydrogel sample, sufficient magnetic beads would be dispersed throughout the gel, allowing for a greater area of the system to be tested. A working solution of 300 μ L of the acrylamide/bis-acrylamide solution was degassed in a vacuum chamber for twenty minutes to reduce oxygen within the solution which prevents polymerization. While the working solution degassed, a 10% ammonium persulfate solution was prepared by measuring 10 mg of ammonium persulfate (VWR) and dissolving it in 100 μ L of ddH₂O.

Table 1:²⁵ Four different concentrations of stock solutions used to make polyacrylamide hydrogels of varying elasticities. The highest and lowest Young's Moduli shown in the table were chosen to reflect values found in literature. The volume of ddH₂O in the table is adjusted so that adding the appropriate concentration of magnetic beads will not dilute the solution.

Final Acrylamide/Bis %	40% Acrylamide (μ L)	2 % Bis (μ L)	ddH ₂ O (μ L)	Young's Modulus \pm Std. Dev. (kPa)
8/0.02	1000	50	3400	1.61 ± 0.11
3/0.10	375	250	3875	1.10 ± 0.34
3/0.06	375	150	3975	0.48 ± 0.16
3/0.03	375	75	4050	0.20 ± 0.03

Next, a microchamber is prepared for the hydrogel to polymerize within so that it can be imaged and visualized under a fluorescent microscope. Calipers and a diamond marker pen (SPI Supplies, West Chester, Pennsylvania) were used to mark the center of the length of treated slides, so that the chamber can be positioned in the same location every time. Three strips of double-sided tape (CVS Pharmacy, Lowell, MA), of 80 μ m thickness each, were placed along the short side of the slides at a width that the coverslips could sit atop. This was done to give the chamber sufficient depth that the beads would be suspended in. A treated coverslip was then placed on the double-sided tape, centered on the center mark, before the tape was trimmed off around the coverslip.

Once the working solution was degassed for twenty minutes, it was removed from the chamber and 33.3 μ L of yellow-green fluorescent magnetic beads of 45 μ m diameter (Spherotech, Lake Forest, Illinois) was added and vortexed in. Finally, 0.50 μ L of tetramethylethylenediamine (TEMED, VWR) and 1.667 μ L of the 10% ammonium persulfate solution were added to initiate gel polymerization. Quickly, the solution was mixed and then applied to the edge of the microchamber, allowing the capillary action to spread the solution

throughout under the coverslip. Clear nail polish was then used to seal the gel edges and lock the chamber. The gels were left to polymerize in a dark location at room temperature for at least 30 minutes to complete the polymerization reaction.

Experimental Setup with Magnet and Imaging Process

The electromagnet used to deliver magnetic force to the system consisted of a soft iron core of 6.35 mm, wrapped 393 times around by 24 AWG magnet wire (Belden, St. Louis, Missouri). An electromagnet was initially chosen as it was thought to be the easiest way to obtain repeatable results; the magnet would not need to be moved during trials and could be controlled by a DC solid state relay (Futurlec, New York, New York) that was triggered through a Labview Software program to supply 9.75A current from a DC power source (GW Instek, Chino, California). With the ability of the electromagnet to deliver and remove forces to the system instantaneously, viscoelastic, time-dependent displacement response could be minimized. Figures 3 and 4 show the electromagnet experimental setup and the control system, respectively. A Neodymium Rare-Earth bar magnet (N50, 0.25 x 0.25 x 1 in; Applied Magnets, Plano, Texas) was also used in experimentation, producing a 1.45 Tesla magnetic field. The hydrogel sample rested on a fixture made of ABS thermoplastic that also held the electromagnet. A clamp, to ensure that neither the sample nor the magnet moved during experimentation, was screwed into the fixture and base of the microscope. The bar magnet used a modified fixture, shown in Figure 5, to allow the magnet to be introduced and removed from the system quickly. The engineering drawing with the dimensions of this modified fixture are included in Appendix A. The displacements of the beads when the magnetic force was applied to the system were viewed using a 10X objective lens with an IX71 Olympus Epifluorescent Microscope (Olympus, Center Valley, Pennsylvania) and imaged with a high speed CCD camera (Cooke Sensicam, PCO, Romulus,

MI). The magnetic beads excite at a wavelength of 488 nm and emit at 520 nm, and the 10X objective has a resolution of 641.97 nm/pixel. CamWare software (PCO) was used to control the high speed camera to focus on beads and capture images over the entire length of each trial. From there, another Labview program that tracks the centroid of each bead based on the intensity of light in each frame, with a resolution to a tenth of a pixel, yielded data of displacement versus time for each trial.

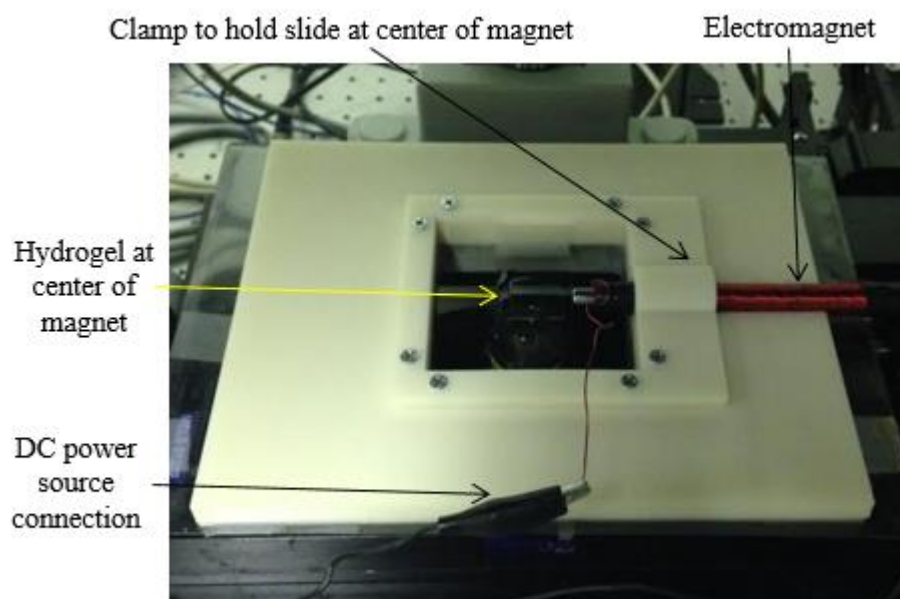


Figure 3: Electromagnet and hydrogel sample held by fixture and clamp on microscope stage and connected to power supply.

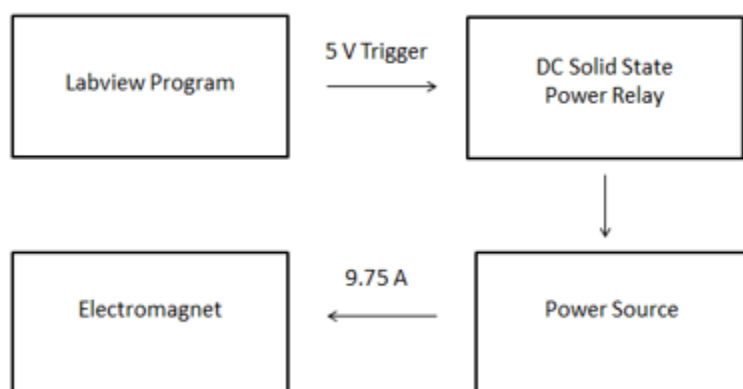


Figure 4: Electromagnet control setup. Upon starting the Labview program, a 5 V trigger is sent to the relay, which activates the power supply to deliver 9.75 A to the electromagnet.

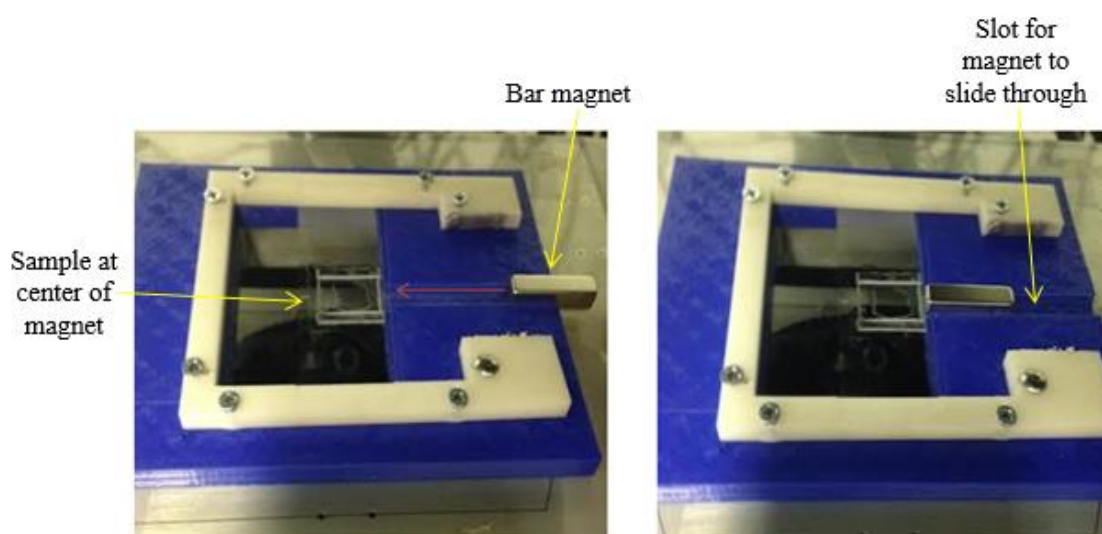


Figure 5: Bar magnet and hydrogel sample held by fixture and clamp on microscope stage. During trials, the bar magnet was slid through the fixture to rest next to the sample, and removed in the same way.

Experimental Testing of Polyacrylamide Hydrogels

Once the electromagnet was placed into the fixture, screwed into the microscope stage, and connected to the power supply (Figure 3), experimental trials could be conducted. Trials using the electromagnet were conducted in the following manner:

- Seconds 1-3: Steady state reading where the electromagnet was not turned on so that the noise of the system was captured.
- Seconds 4-7: The electromagnet was turned on causing force on the beads.
- Seconds 8-10: The electromagnet was turned off while the response of the beads was still monitored.

When testing with the bar magnet, a similar trial setup was followed as with the electromagnet. The bar magnet was manually placed into the fixture and slid to and away from the sample. Trials with the bar magnet were conducted for a longer period of time than with the electromagnet because of the extra time necessary to physically move the magnet. Thus, trials using the bar magnet were conducted in the following manner:

- Seconds 1-3: Steady state reading where the bar magnet was not introduced to the system so that the noise of the system was captured.
- Seconds 4-5: The bar magnet was picked up, placed into the fixture, and slid to the left so that it rested right next to the sample, causing force on the beads.
- Seconds 6-9: The bar magnet was left to sit next to the sample, and the response of the beads to a constant magnetic field was recorded over the three seconds.
- Seconds 10-15: The bar magnet was slid out of the fixture while the response of the beads was still monitored.

The delay time and amount of exposure in the CamWare software settings was adjusted to provide a good balance between a clear image of the bead relative to the background and also having a sufficient number of frames per second of image capture. Three runs per each position were recorded so that a sample size of three could be used to average the displacement of each bead.

Determination of Bead Position

In order to determine the positions of each image taken, a coordinate axis with an origin first needed to be defined. Figure 6 shows how the origin was set as the bottom corner of the coverslip on the magnet side of the system, from which all other coordinates would be referenced.

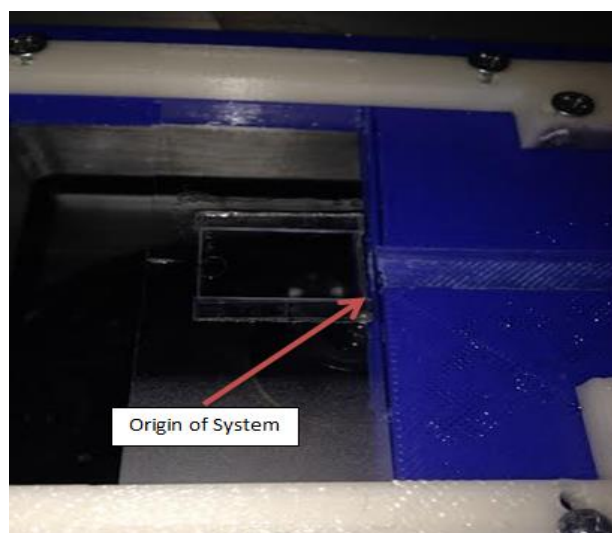


Figure 6: Corner of microscope slide defined as origin of entire system. Vernier scale readings for each image and bead position are referenced against the coordinates of the origin to give a coordinate point that lies within the working range of the system.

At the beginning of any experiment, the origin was located and the values on the vernier scales (± 0.001 mm) of the microscope stage (Mad City Labs, Madison, Wisconsin) were recorded for the x-direction and y-direction. From there, the stage position values were recorded before each trial and referenced to the origin's stage position values. Positions to be imaged were kept well within the working range of the system, shown in Figure 7, so that boundary conditions had no influence. Because the beads are randomly dispersed throughout a sample, the position coordinates from one sample to another are different; there is no set order in which positions are imaged. For example, the first position of the first sample tested will not be in the same location as the first position of the second sample tested. A wide range of positions across the working

range of the sample was ideally tested during each experiment, but again, this was contingent on where the beads were fixed in the sample.

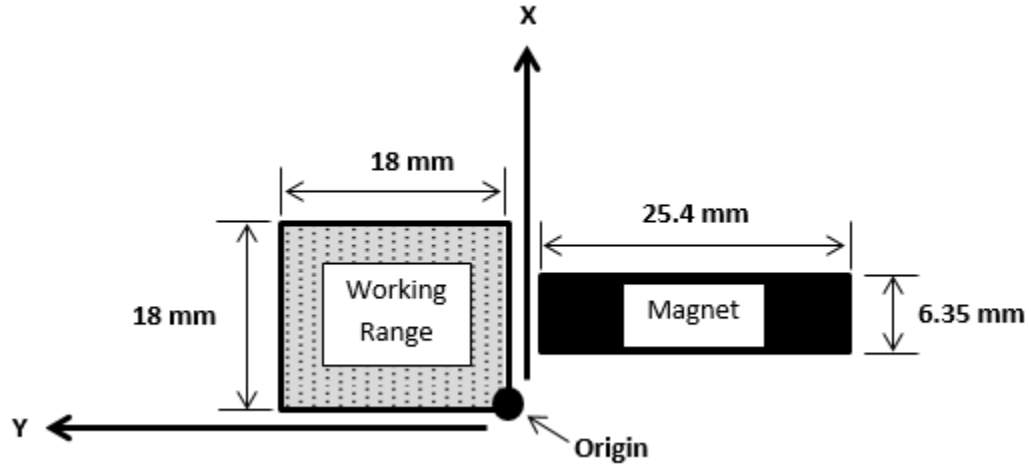


Figure 7: Diagram of the system with dimensions showing the working range of the system relative to the bar magnet. The axes orientations are defined based off of CamWare assigning displacement to the left (away from the magnet in the experimental setup) as positive, and displacement upward as positive. The axes orientations were necessary for use in calculating the bead positions for images with multiple beads.

In the case of a single bead being present in the image, the scales were adjusted so that the bead appeared in the center of the image, and the coordinate of that position was then assigned to the bead. If more than one bead was present, then the recorded position was assigned as the location of the bead closest to the center of the image. The program, ImageJ, was used to determine the position of other beads in the image frame relative to the reference center bead by measuring the distances between them. An example of this process is shown in Figure 8.

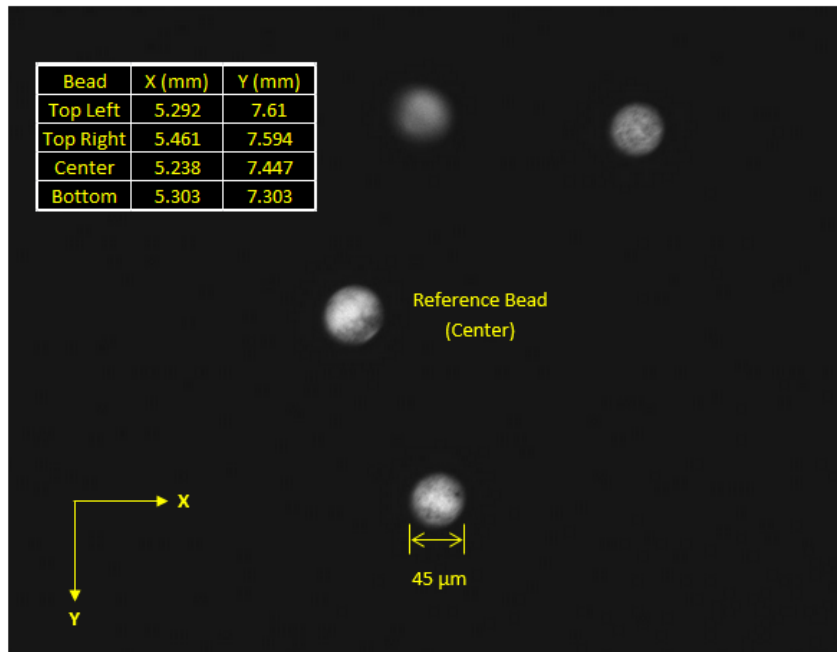


Figure 8: Image of one position with three beads in the frame. The coordinates of the center bead were determined from the readings on the vernier scales of the stage, relative to the defined origin. The coordinates of the beads above and below the center bead were found by measuring their distance from the referenced center bead using ImageJ software.

Data Analysis, Testing, and Optimization of Experimental Setup

The Labview tracking software outputs an Excel file of raw data for each bead in one position image of the beads' x and y displacement. This raw data was then plotted as displacement across time in order to see the response type of the beads. The time scale was determined by noting the number of frames per second (FPS) that the CamWare image capture software was sampling at during image acquisition, taking the reciprocal of the FPS, and adding this time step for each sequential displacement data point.

The results of displacement of the beads during experimental testing with the electromagnet and bar magnet did not show consistent elastic responses. The majority of the bead responses exhibited a displacement plot like those of Figure 9 below.

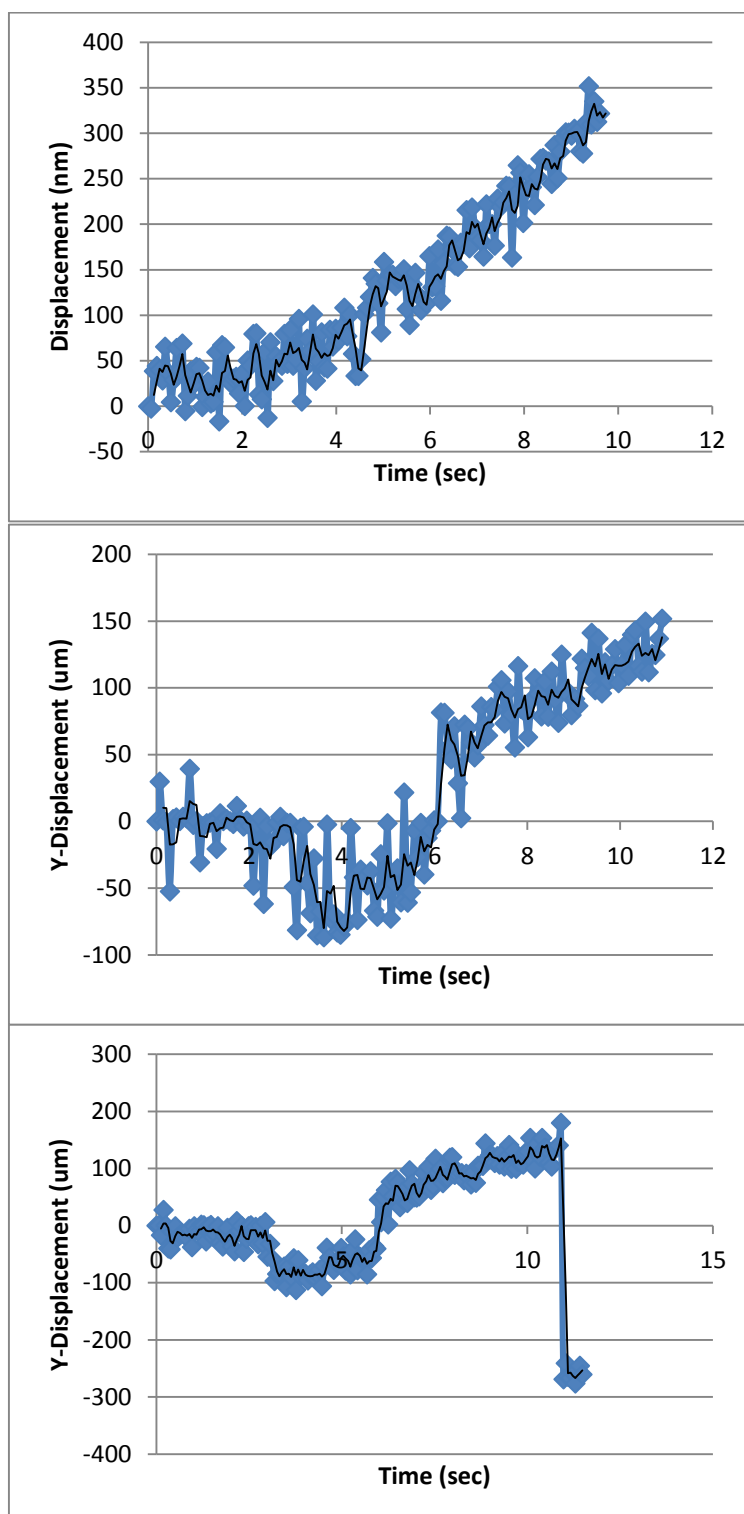


Figure 9: Common displacement traces of beads in a hydrogel during a trial.

The unintuitive and inconsistent nature of these responses meant that factors within the system existed that were preventing the beads from displacing in an elastic fashion. This led to an in-depth analysis of the system; Hooke's Law cannot be applied and the magnetic force field in the working range of the system cannot be determined unless the displacement responses are linearly elastic. The first change made was in the design of the electromagnet fixture, which held the hydrogel sample in place in line with the bottom of the magnet, rather than the center axis. Because of this, the beads within the hydrogel were subjected to magnetic field fringe effects in the z-direction, and thus, would have displacement in that direction. With the current software and imaging setup, displacement in the z-direction cannot be measured. In order to negate the effects of the magnetic field in the z-direction, modifications were made to the fixture to raise the hydrogel sample 3.175 mm higher, half the diameter of the magnet. Figure 10 shows how the sample was raised to rest in line with the center of the magnet.

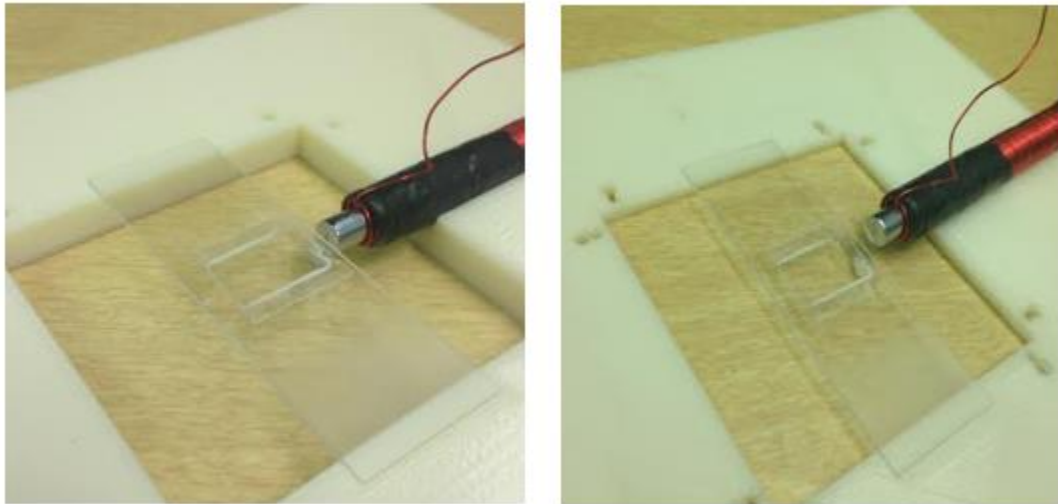


Figure 10: Modification to the fixture to raise the hydrogel sample to rest in line with the center of the electromagnet. The figure on the left shows the improved fixture, while the figure on right shows the previous fixture, where the hydrogel sample rested in line with the bottom of the electromagnet.

Next, experiments were run with samples consisting of beads in a solution of 55% ddH₂O and 45% glycerol prepared under a microchamber, like that of the hydrogel, and tested against the electromagnet. These trials were conducted because the high viscosity of glycerol would cause resistance to the motion of the beads, while still allowing a much larger displacement than the hydrogels that could be visible to the naked eye. While watching the beads displace live from the CCD camera, the beads began rotating more so than they displaced when the electromagnet was turned on. This indicated that the beads were touching and adhering to the surface of the glass slide. This was a result of the sample slides left resting flat during the polymerization process, causing the beads of greater density than the gel to settle to the bottom on the surface of the slide before the gel finished polymerizing. The magnetic beads were not suspended in the gel as was originally thought. To remedy this issue, a small device, shown in Figure 11, consisting of a base with a motor and fixture to hold the sample was machined so that during the polymerization process, the slide could be kept in constant rotation.

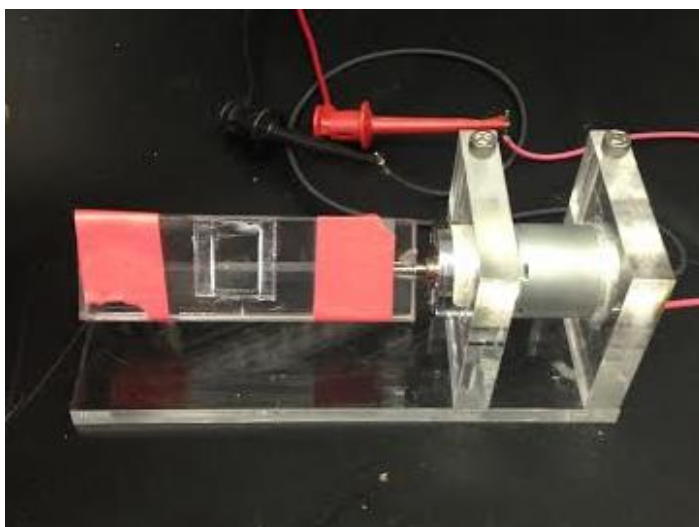


Figure 11: Fabricated motor-device for rotation of the sample. The motor-device when connected to a power source rotates the sample during the polymerization reaction to prevent beads from sinking to the bottom of the sample and ensuring dispersion of beads throughout the gel.

Inclusion of this would prevent the beads from settling to the bottom of the slide during the polymerization reaction, as the direction of gravity relative to the beads would constantly be changing. This inclusion of rotating the sample was proven successful at preventing the beads from settling on the surface of the slide; Figure 12 shows multiple beads embedded in the hydrogel at different depths when viewed under the fluorescent microscope. This eliminated the problem of beads touching the surface of the glass slide and affecting displacement. Beads within the hydrogel were measured to have differences in depth up to approximately 70 microns.

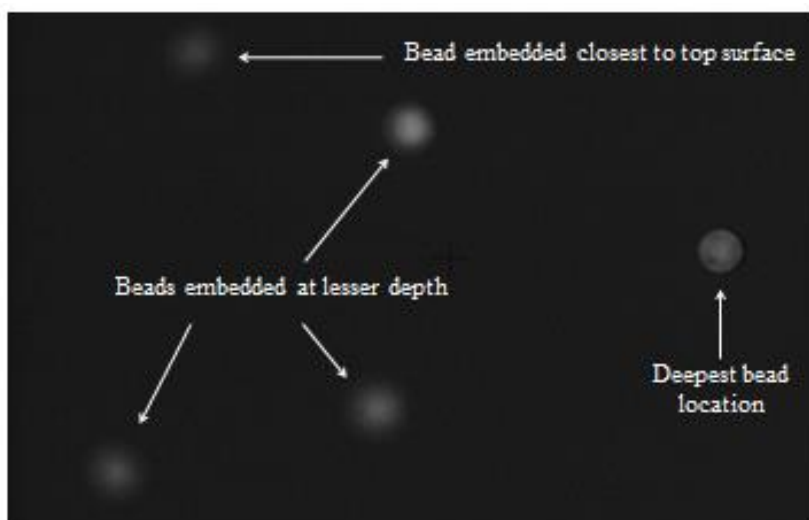


Figure 12: Image of magnetic beads embedded in hydrogel. The bead furthest to the right is embedded deepest within the hydrogel as compared to the others, as the image appears as a focused circle. Conversely, the bead in the top left corner is embedded closest to the surface, as the resolution of its image is the least clear.

Another area of concern was the amount of heat transfer in the system; the electromagnet after just one trial of having current flow around the iron core heats up to significantly high temperatures. If the heat dissipates from the electromagnet and spreads to the plastic of the fixture and clamp, the possibility of thermal expansion causing the fixture to expand and move the sample exists. Using a digital thermometer (Keithley, Solon, Ohio), various points around the

system, illustrated in Figure 13, were monitored for temperature increase while the electromagnet was turned on.

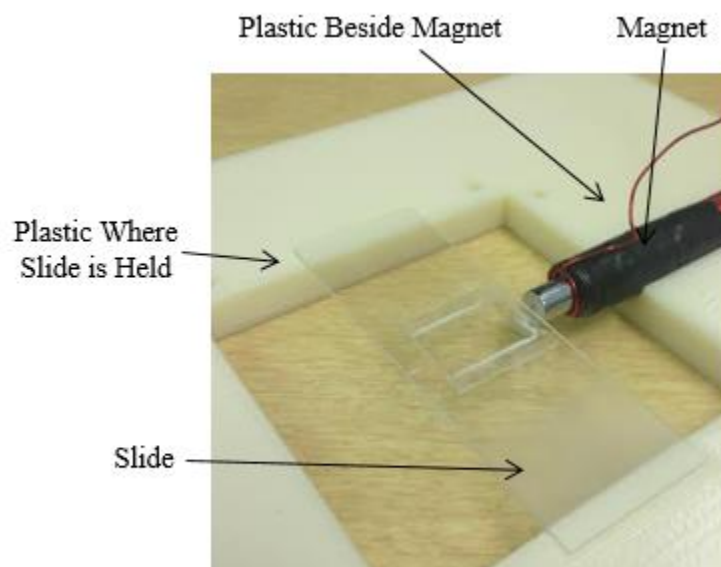


Figure 13: Locations where temperatures were measured in the system.

However, the data in Table 2 showed that the temperature increase was no more than a couple of degrees anywhere in the system, which would not cause any significant expansion in the plastic or viscosity change in the hydrogel.

Table 2: Temperature increase at various points in the system due to heat dissipated from the electromagnet.

Temperatures of Various Points in System (F)				
Pull	Magnet	Plastic Beside Magnet	Plastic Where Slide is Held	Slide
0	78	78.4	78.1	78.1
1	88	80.1	78.1	78.1
2	96.5	81.7	78.1	78.1
3	100.1	82.6	78.1	78.1
4	107.1	86.4	78.2	78.1
5	109	87.7	78.2	78.2
6	113	87.8	78.2	78.2
7	113.2	89.1	78.2	78.3
8	112.5	87.7	78.2	78.3
9	114.6	86.5	78.2	78.3

Even after taking these steps, elastic displacement responses of the magnetic beads induced from the electromagnet were not achieved consistently. Because the displacement responses using the bar magnet were just as inconsistent and non-elastic in nature, the issue appeared to lie in the bead-hydrogel interaction, rather than the mode of force application. The magnetic beads were never actively bound to the hydrogel cross-linkages; they were simply added and assumed to move against the resistance of the gel. At this point, the troubleshooting of the electromagnet and hydrogel system was set aside to pursue a new methodology.

Drag Force

Measuring the drag force of magnetic beads moving through a viscous medium is another approach to mapping the magnetic field within the system. Equation 2 provides the relationship between the drag force (F_D) exerted on an object moving through a fluid, the object's velocity (v), and a characteristic drag coefficient (C_D).

$$F_D = C_D * v \quad (\text{Equation 2})$$

In the case of this experiment, the expressions of Stoke's drag (Equation 3) and the corresponding drag coefficient (Equation 4) were used; Stoke's drag quantifies the frictional force on a small sphere moving through a viscous fluid as a function of the fluid viscosity (μ) and particle radius (R) and velocity (v).

$$F_D = 6 * \pi * \mu * R * v \quad (\text{Equation 3})$$

$$C_D = 6 * \pi * \mu * R \quad (\text{Equation 4})$$

When applying the Stoke's drag equation, the following assumptions are made:²⁷

- Laminar flow
- Low Reynolds number flow
- Particles are spherical in shape
- Particles do not interfere with one another
- Medium is homogenous and continuous in all directions

The first four assumptions above are valid in the case of the conditions of this experiment, as the magnetic beads are small in diameter and move at low velocities, as shown in Table 4. However, the medium of the beads cannot be considered continuous, as a boundary condition is introduced when the beads come into contact with the surface of the glass slide. In previous experiments using optical tweezers, spherical beads have been used to study the mechanical properties of biological material; in many cases, these experiments are performed near a plane surface such as a glass coverslip.²⁸ The static and dynamic forces between the beads and the surface can profoundly influence the outcomes of these experiments.²⁸ As such, a correction factor was used in calculations of force based on the velocity of bead motion.

Faxen's Law

The correction factor was calculated using Faxen's Law, which relates a sphere's velocity and angular velocity to the forces and torques experienced under low Reynolds number flow.²⁸

Equation 5 shows a numerical approximation of Faxen's Law; the corrected lateral drag coefficient (C_F) is a function of the Stoke's drag coefficient (C_D), the radius of the particle (R), and the distance from the center of the particle to the surface of a sample (h). Figure 14 illustrates the effect of increasing h on C_F .

$$C_F = \frac{C_D}{1 - \frac{9R}{16h} + \frac{R^3}{8h^3} - \frac{45R^4}{256h^4} + \frac{R^5}{16h^5}} \quad (\text{Equation 5})$$

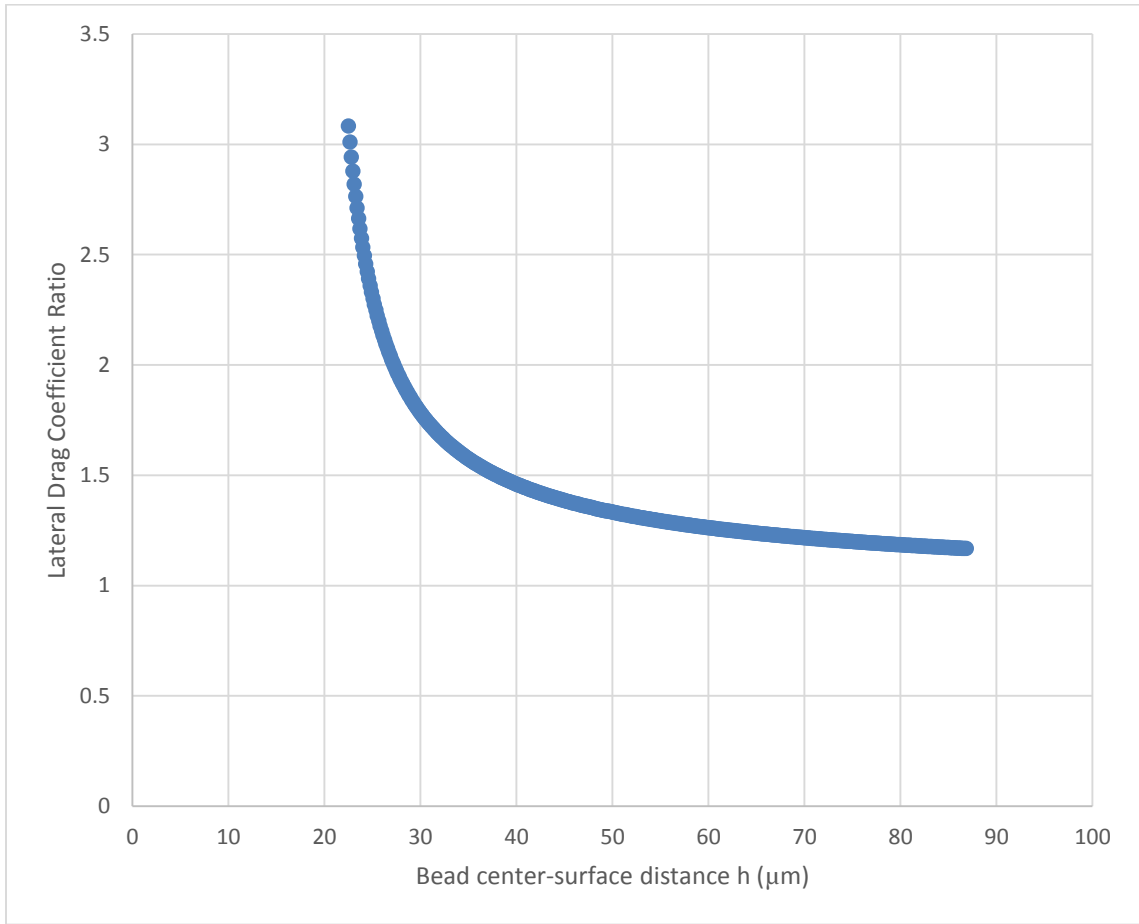


Figure 14: Faxen's Law. Equation 5 exhibits the ratio of the corrected drag coefficient to the Stoke's drag coefficient as a function of the distance from the bead center to the surface of the glass slide for a particle with radius of $22.5 \mu\text{m}$. This ratio serves as a correction factor to be applied to the Stoke's drag force equation. As the bead moves further away from the surface, the correction factor decreases towards an asymptote of one.

Assuming that the distance from the center of the bead to the surface is only equal to the radius of the bead, the value of the correction factor is 3.08. Thus, the modified Stoke's equation (Equation 6) corrected to solve for drag force was obtained.

$$F_D = 3.08 * 6 * \pi * \mu * R * v \quad (\text{Equation 6})$$

Experimentation with Viscous Fluid

Applying the bar magnet to the system will induce constant motion in the magnetic beads, and the resistance to this motion is equivalent to the magnetic force at that location. The magnetic beads were mixed in various solutions of differing concentrations of glycerol and albumin solution (1% w/v). The viscosity of the prepared solution was then measured using a cylindrical viscometer (Vilastic Scientific, Austin, Texas). A microchamber for the sample was prepared in the same way as the hydrogels were, with the bead solution being contained between a microscope slide and a coverslip. The process of image capture using the fluorescent microscope and CamWare software, and applying the bar magnet using the same fixture as above, also did not change. However, the Labview particle tracking program was unable to resolve, track, and calculate displacements on the order of microns; previously, displacement in the hydrogels were on the order of nanometers. Because of this, the plugin Multitracker in ImageJ software was used to track displacements over time. The plugin works by identifying the movement of objects through a binary image stack through distinguishing pixels with light intensity and pixels with no light intensity. For each image in the stack, a pixel coordinate is assigned to each particle in the image; converting these pixel values to microns based on the camera resolution yields tracked displacement. This data is outputted to an Excel file and graphed on a scatterplot.

Bovine Blood Preparation and Thrombus Formation

Bovine blood was obtained from the Penn State Dairy Farm (IACUC No. 46269); each collection bag contained 450 mL of blood taken from the jugular vein of a cow, with 63 mL of citrate phosphate dextrose adenine (CPDA-1) added as an anticoagulant. To counteract the anticoagulant and reinitiate clotting of the bovine blood, 6.45% calcium chloride was added at the

ratio of 1 mL calcium chloride per 50 mL of blood. From there, 300 μL of blood was mixed with 33 μL of the magnetic bead solution; a microchamber for the sample, shown in Figure 15, was then created by injecting the solution between a coverslip and microscope slide in the same way as was performed when using the hydrogels. Samples were left on a rocking stand and tested only after the clotting process was complete. The clotting process was verified to be complete by placing a test tube containing blood on the rocking stand as well and seeing when the blood was completely coagulated and no longer liquid. The imaging and tracking process used when experimenting with blood clots followed the same procedure previously detailed when experimenting with hydrogels.



Figure 15: Prepared bovine thrombus sample.

A definitive feature of hemostasis and thrombosis is that platelets generate contractile forces that retract the thrombus' size and strengthen its adhesion to the exposed matrix after adhering and aggregating at the wound site.²⁹ Although the magnitude of these contractile forces is not fully understood, the fact that they exist could impact the displacement responses of the beads observed in the clot. As a result, to explore whether platelets had any contractile resistance to bead deformation, blood clots containing only the platelet-enriched plasma and blood clots containing only the packed red blood cells were tested. In order to extract the platelet-rich plasma (PRP) and packed red blood cells (RBC), 45 mL of whole bovine blood was centrifuged at 1800 revolutions per minute for fourteen minutes. The top layer containing the PRP and the layer

below containing the white buffy coat was then removed using a pipette and expelled into a fresh test tube. The remaining bovine blood was then centrifuged again, this time at 3600 revolutions per minute for twenty minutes. The packed RBC layer was then drawn up from the bottom-most layer and transferred to a fresh test tube. The PRP and white buffy coat solution and the packed RBC solution were then made into samples between a microscope slide and coverslip with the magnetic beads following the same procedures as detailed previously.

Studying the varying localized elasticities throughout a thrombus is the ultimate goal of this project; the formation of a thrombus *in vivo* can be simulated through a mock circulatory loop containing a backward-facing step geometry that induces flow separation. However, before proceeding to experimentation with clots formed within the flow loop, a prudent measure was taken to first verify that elastic deformation and constant elasticities could be observed and calculated in a uniform thrombus medium, where the results should not vary across the material. Rather than forming the clot in a flow loop, where it would form layer by layer in an uneven manner, the samples were prepared and left to clot in the microchamber of a microscope slide and coverslip. It was assumed that in this way, the blood clot would be relatively uniform throughout and if the results were repeatable, then thrombi formed in a manner closely resembling *in vivo* conditions could be tested.

Chapter 3

Results

Bar Magnet Testing in Viscous Fluid

Initially, a fluid with viscosity of 2.1 cP was used to calculate force values within the working range of the system. Three different samples of this fluid, rather than just a single

sample, were tested during the experiment, to verify that there was insignificant variation between samples; the force values calculated for each position in each sample should be comparable to one another. Testing the first sample, data was collected at 21 positions within the working range of the system containing 34 beads in total. Testing the second and third samples, data was collected at 29 positions containing 51 beads and 29 positions containing 49 beads, respectively. Table 3 shows the bead coordinates relative to the magnet origin for each position imaged of each sample. Note that the position numbers do not correspond to the actual order that positions were tested. The positions were renumbered during post-processing to help keep the data organized based off of the y-coordinate, to better visualize the range of coordinates being tested.

Table 3: Locations of beads in fluid with viscosity of 2.1 cP relative to the magnet origin for (a) Sample 1, (b) Sample 2, and (c) Sample 3. Each position represents a specific location imaged under the fluorescent microscope and all of the beads within that image position analyzed together using tracking software.

(a)

Position	Bead	Y Position (mm)
1	1	15.280
	2	15.280
	3	15.280
	4	15.280
2	1	14.610
3	1	13.550
4	1	13.430
	2	13.430
5	1	12.800
	2	12.800
6	1	12.230
	2	12.230
7	1	11.870
8	1	11.700
	2	11.700
9	1	11.640
10	1	10.540
	2	10.540
11	1	10.060
	2	10.060
12	1	9.514
	2	9.514
13	1	9.220
14	1	9.115
	2	9.115
15	1	9.046
	2	9.046
16	1	8.392
17	1	7.405
18	1	7.386
19	1	7.181
20	1	6.733
21	1	4.768
	2	4.768

Position	Bead	Y Position (mm)
16	1	8.392
17	1	7.405
18	1	7.386
19	1	7.181
20	1	6.733
21	1	4.768
	2	4.768

(b)

Position	Bead	Y Position (mm)
1	1	18.09
2	1	17.78
	2	17.78
3	1	17.05
4	1	16.06
	2	16.06
	3	16.06
	4	16.06
	5	16.06
5	1	15.12
	2	15.12
	3	15.12
	4	15.12
6	1	14.65
	2	14.65
	3	14.65
7	1	14.18
	2	14.18
8	1	13.92
	2	13.92
	3	13.92
9	1	13.67
	2	13.67
10	1	13.64
11	1	13.44
12	1	12.97
13	1	12.53
14	1	12.38
	2	12.38
15	1	10.76
16	1	10.75
17	1	10.36
18	1	9.886
19	1	9.805
20	1	9.521
	2	9.521
21	1	9.292
	2	9.292

Position	Bead	Y Position (mm)
22	1	9.045
23	1	8.838
24	1	7.839
25	1	7.18
26	1	7.171
	2	7.171
27	1	5.827
28	1	5.717
	2	5.717
	3	5.717
	4	5.717
	5	5.717
29	1	5.709

(c)

Position	Bead	Y Position (mm)
1	1	19.74
2	1	19.66
3	1	17.25
	2	17.25
4	1	17.22
	2	17.22
	3	17.22
	4	17.22
5	1	16.91
	2	16.91
6	1	16.45
7	1	15.91
	2	15.91
8	1	15.84
9	1	15.36
	2	15.36
	3	15.36
10	1	14.95
11	1	14.2
	2	14.2
12	1	14.1
13	1	13.93
	2	13.93
14	1	13.73
15	1	13.46
	2	13.46
16	1	12.95
	2	12.95
17	1	12.57
	2	12.57
18	1	12.41
19	1	12.13
20	1	12.03
	2	12.03
21	1	10.89
22	1	9.804
	2	9.804
23	1	9.744

Position	Bead	Y Position (mm)
24	1	8.454
25	1	8.424
26	1	8.17
27	1	7.961
28	1	7.491
29	1	6.966

It is important to note that all data was taken at positions with x-coordinates that rested within the width of the bar magnet. This allowed for the approximation that all displacement was in the y-direction, because there would be no fringing of the magnetic field in the x-direction at a position in line with the axis of the magnet. In order to apply the data collected to the Stoke's drag force equation, constant velocities of beads at each of these positions needed to be obtained. Responses of displacement over time, outputted using the tracking software, verified that beads were indeed moving at constant velocities. Figure 16 shows a representative plot of tracking data obtained from a position containing multiple beads in the image. In this position, four beads were imaged, as exhibited by the four different curves of displacement versus time. The curves generally are linear in shape, corresponding to constant velocity motion of the bead over time. Notice that at times, each curve may exhibit a horizontal section, indicating that the bead was not displacing. During experimentation, beads occasionally were observed to stop moving, likely due to the bead adhering to the glass microscope slide. If this happened during a trial, the sample would be lightly tapped with a screwdriver to dislodge the bead. This tapping of the sample did not affect the displacement of other beads, as the slopes of the displacement curves corresponding to these beads remained constant. A velocity for each bead in the position would thus be calculated by dividing the change in x over the change in y in a continuous linear portion of the curve.

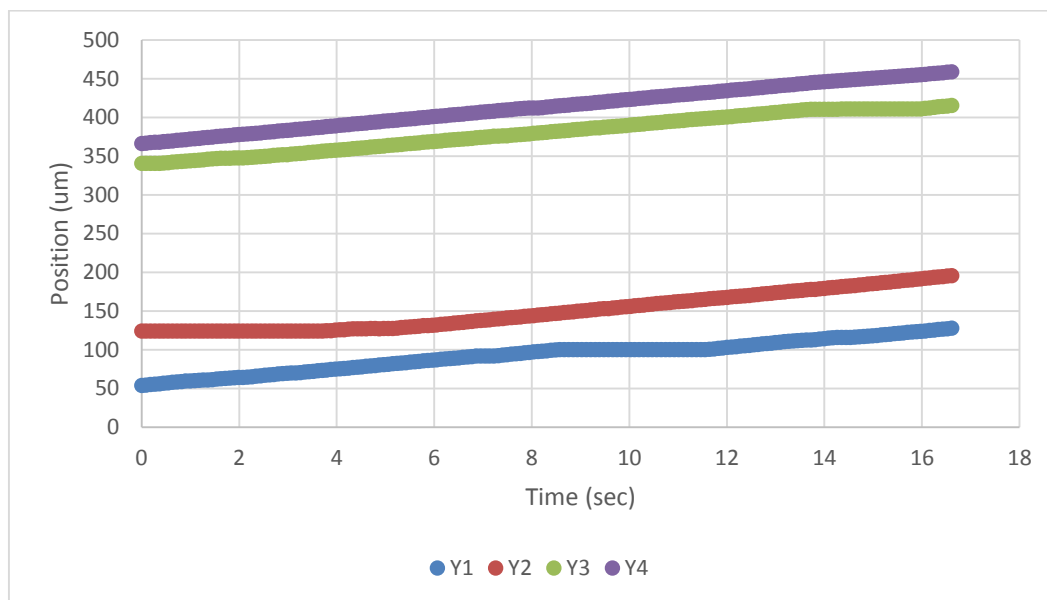


Figure 16: Representative displacement data of one trial at one position containing four beads in the image. Velocity for each bead in the image was calculated by finding the slope of a linear section of the curve. For example, the velocity of bead 1, corresponding to data set Y1 on the plot, was calculated as the slope of the curve from $t=0$ seconds to $t=7$ seconds.

To check whether the data acquired from each sample was consistent, the velocity distributions of all three samples were plotted together, shown in Figure 17. The fact that each sample set of data follows the same non-linear decay trend in velocity as position away from the magnet increases gives confidence that this experimental methodology is repeatable from sample to sample.

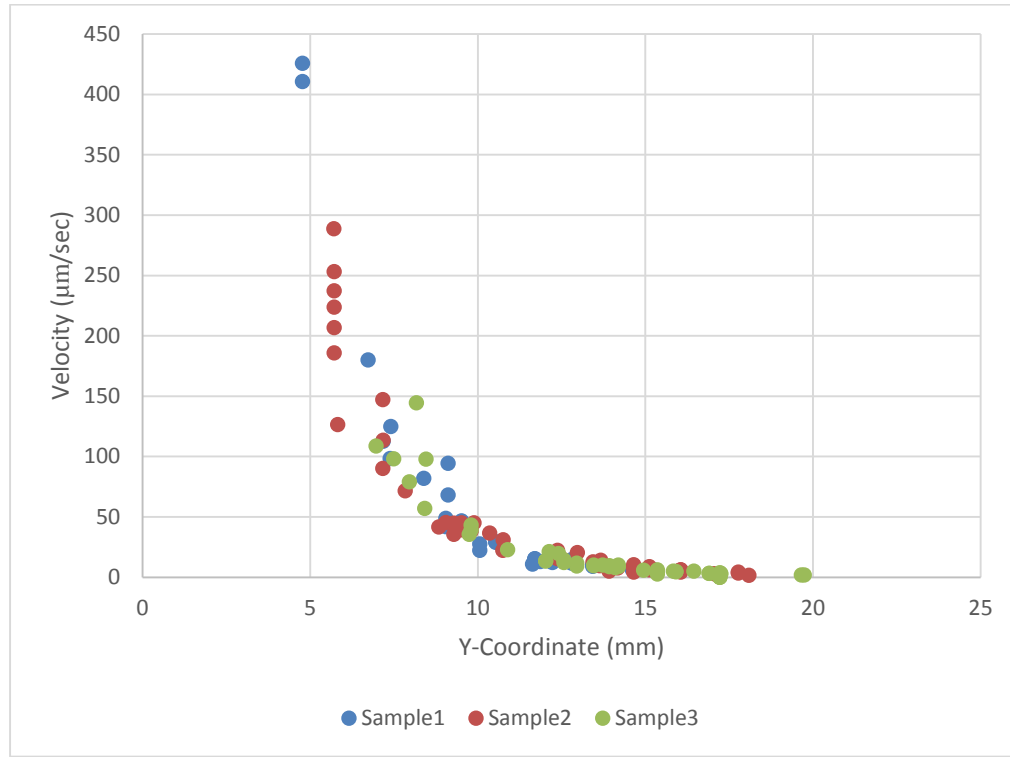


Figure 17: Velocities at various positions within the working range of the system. Velocities for the three data sets taken from testing on the three samples of fluid at 2.1 cP. All data sets for the three samples of fluid at 2.1 cP exhibit the same behavior of non-linear decay in velocity as the position away from the magnet origin increases.

At this point, force values at each position could be calculated using the velocities illustrated above and Equation 6, the modified Stoke's equation.

$$F_D = 3.08 * 6 * \pi * \mu * R * v \quad (\text{Equation 6})$$

Knowing the viscosity μ of the fluid to be 2.1 cP, the radius R of the beads to be 22.5 μm , and the velocity of the bead taken from the tracking plots, force values for each data point could be calculated. Velocities taken from the plots obtained from tracking data and the calculated force values are shown in Table 4 for Sample 1, Sample 2, and Sample 3.

Table 4: Velocity values and calculated magnetic force acting on beads immersed in a 2.1 cP viscosity fluid at specific positions for (a) Sample 1, (b) Sample 2, and (c) Sample 3.

(a) Sample 1

Position	Bead	Y Position (mm)	Velocity ($\mu\text{m}/\text{sec}$)	Force (pN)
1	1	15.280	5.81	15.94
	2	15.280	6.00	16.46
	3	15.280	5.37	14.74
	4	15.280	5.80	15.92
2	1	14.610	6.71	18.41
3	1	13.550	9.88	27.10
4	1	13.430	9.29	25.48
	2	13.430	10.54	28.91
5	1	12.800	11.77	32.29
	2	12.800	14.87	40.79
6	1	12.230	12.28	33.69
	2	12.230	15.63	42.86
7	1	11.870	13.21	36.24
8	1	11.700	15.52	42.58
	2	11.700	15.23	41.78
9	1	11.640	10.96	30.06
10	1	10.540	28.98	79.49
	2	10.540	29.49	80.89
11	1	10.060	22.53	61.80
	2	10.060	27.64	75.82
12	1	9.514	46.72	128.16
	2	9.514	46.41	127.31
13	1	9.220	43.78	120.09
14	1	9.115	94.48	259.17
	2	9.115	68.34	187.46
15	1	9.046	42.09	115.47
	2	9.046	48.97	134.33
16	1	8.392	82.22	225.54
17	1	7.405	125.13	343.25
18	1	7.386	98.57	270.39
19	1	7.181	112.86	309.59
20	1	6.733	180.24	494.42
21	1	4.768	410.72	1126.64
	2	4.768	425.93	1168.37

(b) Sample 2

Position	Bead	Y Position (mm)	Velocity ($\mu\text{m}/\text{sec}$)	Force (pN)
1	1	18.090	1.68	4.61
2	1	17.780	4.51	12.37
	2	17.780	3.62	9.93
3	1	17.050	3.05	8.37
4	1	16.060	4.32	11.85
	2	16.060	6.37	17.47
	3	16.060	5.79	15.88
	4	16.060	6.35	17.42
	5	16.060	5.39	14.79
5	1	15.120	6.31	17.31
	2	15.120	6.86	18.82
	3	15.120	9.04	24.80
	4	15.120	7.04	19.31
6	1	14.650	10.63	29.16
	2	14.650	7.77	21.31
	3	14.650	4.57	12.54
7	1	14.180	7.76	21.29
	2	14.180	9.28	25.46
8	1	13.920	7.58	20.79
	2	13.920	5.26	14.43
	3	13.920	8.90	24.41
9	1	13.670	11.61	31.85
	2	13.670	14.18	38.90
10	1	13.640	9.74	26.72
11	1	13.440	12.98	35.61
12	1	12.970	20.49	56.21
13	1	12.530	15.06	41.31
14	1	12.380	22.48	61.66
	2	12.380	15.66	42.96
15	1	10.760	31.15	85.45
16	1	10.750	22.35	61.31
17	1	10.360	36.88	101.17
18	1	9.886	45.17	123.91
19	1	9.805	38.38	105.28
20	1	9.521	45.35	124.40
	2	9.521	39.37	108.00
21	1	9.292	35.76	98.09

	2	9.292	45.09	123.69
22	1	9.045	45.46	124.70
23	1	8.838	41.81	114.69
24	1	7.839	71.71	196.71
25	1	7.180	113.68	311.84
26	1	7.171	90.35	247.84
	2	7.171	147.30	404.06
27	1	5.827	126.60	347.28
28	1	5.717	185.99	510.19
	2	5.717	206.96	567.71
	3	5.717	237.53	651.57
	4	5.717	253.46	695.26
	5	5.717	223.82	613.96
29	1	5.709	288.77	792.12

(c) Sample 3

Position	Bead	Y Position (mm)	Velocity ($\mu\text{m}/\text{sec}$)	Force (pN)
1	1	19.740	2.14	5.86
2	1	19.660	2.16	5.94
3	1	17.250	2.92	8.01
	2	17.250	3.35	9.18
4	1	17.220	3.84	10.53
	2	17.220	0.33	0.90
	3	17.220	0.29	0.80
	4	17.220	0.32	0.86
5	1	16.910	3.26	8.94
	2	16.910	3.41	9.35
6	1	16.450	5.21	14.28
7	1	15.910	4.58	12.55
	2	15.910	4.90	13.44
8	1	15.840	5.23	14.35
9	1	15.360	2.75	7.54
	2	15.360	4.75	13.03
	3	15.360	6.36	17.44
10	1	14.950	6.01	16.48
11	1	14.200	8.99	24.66
	2	14.200	10.33	28.34
12	1	14.100	8.11	22.24
13	1	13.930	9.02	24.73

	2	13.930	9.76	26.76
14	1	13.730	10.33	28.34
15	1	13.460	10.29	28.24
	2	13.460	9.69	26.58
16	1	12.950	11.89	32.60
	2	12.950	9.38	25.74
17	1	12.570	12.40	34.01
	2	12.570	14.44	39.61
18	1	12.410	19.73	54.13
19	1	12.130	21.44	58.80
20	1	12.030	13.82	37.90
	2	12.030	13.82	37.90
21	1	10.890	23.08	63.30
22	1	9.804	43.44	119.17
	2	9.804	39.45	108.21
23	1	9.744	35.79	98.17
24	1	8.454	97.90	268.55
25	1	8.424	57.08	156.58
26	1	8.170	144.69	396.90
27	1	7.961	79.29	217.51
28	1	7.491	98.29	269.61
29	1	6.966	108.79	298.41

After the first experiment was complete, it was realized that not enough data of positions 5 mm and closer to the magnet origin had been acquired. This was due to the fact that at positions within 5 mm of the magnet, beads were moving through the image pane at velocities so fast that the camera could not take a sufficient number of images in time. Thus, additional experiments needed to be conducted of testing beads in a fluid of higher viscosity. This would increase the resistance towards bead movement, so that the velocities of beads at positions very close to the magnet would be lower and capable of imaging. Two more samples of beads, Sample 4 and Sample 5, immersed in a fluid with viscosity of 12 cP were subsequently tested, with the results of velocity and force shown in Table 5.

Table 5: Velocity values and calculated magnetic force acting on beads immersed in a 12 cP viscosity fluid at specific positions for (a) Sample 4 and (b) Sample 5.

(a) Sample 4

Position	Bead	Y Position (mm)	Velocity ($\mu\text{m/sec}$)	Force (pN)
1	1	0.953	337.80	5334.18
	2	0.953	420.60	6641.67
	3	0.953	240.90	3804.04
	4	0.953	310.20	4898.35
	5	0.953	212.90	3361.89
2	1	1.447	233.20	3682.45
3	1	1.543	230.40	3638.24
	2	1.543	286.00	4516.21
	3	1.543	287.10	4533.58
	4	1.543	182.90	2888.17
4	1	2.187	237.50	3750.35
	2	2.187	314.50	4966.25
	3	2.187	384.30	6068.46
	4	2.187	297.80	4702.55
5	1	2.401	153.00	2416.02
	2	2.401	123.60	1951.76
	3	2.401	122.96	1941.66
	4	2.401	132.96	2099.57
	5	2.401	154.00	2431.81
6	1	2.464	183.30	2894.48
7	1	2.507	192.70	3042.92
	2	2.507	100.30	1583.83
	3	2.507	144.60	2283.37
8	1	2.511	151.15	2386.80
	2	2.511	173.00	2731.83
9	1	2.571	115.50	1823.86
10	1	2.656	151.70	2395.49
	2	2.656	137.70	2174.41
	3	2.656	158.60	2504.45
	4	2.656	202.96	3204.93
	5	2.656	157.60	2488.65
	6	2.656	141.20	2229.68
	7	2.656	133.60	2109.67
	8	2.656	123.90	1956.50
	9	2.656	117.60	1857.02

11	1	2.871	107.60	1699.11
12	1	2.885	125.90	1988.08
	2	2.885	119.90	1893.34
	3	2.885	139.60	2204.42
13	1	2.922	111.16	1755.27
14	1	2.942	86.80	1370.65
	2	2.942	110.10	1738.58
	3	2.942	158.50	2502.87
	4	2.942	134.00	2115.99
15	1	2.997	118.77	1875.51
16	1	3.008	102.20	1613.84
	2	3.008	117.30	1852.28
	3	3.008	112.90	1782.80
	4	3.099	96.20	1519.09
	5	3.099	92.70	1463.82
	6	3.099	76.90	1214.32
17	1	3.137	64.20	1013.78
	2	3.137	77.40	1222.22
18	1	3.157	91.74	1448.68
19	1	3.185	74.06	1169.53
	2	3.185	103.51	1634.55
20	1	3.19	88.80	1402.24
21	1	3.332	145.50	2297.58
	2	3.332	158.10	2496.55
22	1	3.442	71.00	1121.16
	2	3.442	79.80	1260.12
	3	3.442	71.20	1124.32
23	1	3.454	72.26	1140.98
24	1	3.486	7.25	114.44
	2	3.486	6.72	106.06
	3	3.486	7.24	114.36
	4	3.486	8.43	133.19
	5	3.486	7.19	113.60
25	1	3.605	29.20	461.10
	2	3.605	70.90	1119.58
26	1	3.632	63.50	1002.80
27	1	3.68	72.80	1149.58
28	1	3.718	70.20	1108.52
	2	3.718	89.80	1418.03
29	1	3.719	109.31	1726.07

	2	3.719	121.20	1913.92
30	1	3.72	68.70	1084.84
31	1	3.982	74.15	1170.90
	2	3.982	69.50	1097.47
32	1	3.933	29.47	465.31
33	1	4.287	69.22	1093.06
	2	4.287	48.62	767.69
	3	4.287	99.27	1567.53
	4	4.287	67.68	1068.71
	5	4.287	57.68	910.76
	6	4.287	55.78	880.85
34	1	4.234	46.80	739.02
35	1	4.408	47.04	742.81
36	1	4.691	43.36	684.72
	2	4.691	40.33	636.78
37	1	4.732	3.51	55.45
	2	4.732	3.88	61.34
	3	4.732	3.40	53.65
38	1	4.815	41.50	655.32
39	1	4.948	16.23	256.26
	2	4.948	24.00	378.99
40	1	4.956	34.23	540.48
41	1	4.959	34.44	543.85
	2	4.959	30.98	489.18
42	1	5.063	30.70	484.78
	2	5.063	30.90	487.94
	3	5.063	32.10	506.89
	4	5.063	33.40	527.42
43	1	5.071	32.08	506.57
	2	5.071	44.90	709.01
	3	5.071	40.06	632.59
	4	5.071	40.84	644.90
	5	5.071	32.79	517.79
	6	5.071	38.28	604.48
44	1	5.21	15.70	247.92
45	1	5.275	2.36	37.33
	2	5.275	0.98	15.42
46	1	5.364	47.44	749.12
	2	5.364	38.25	604.01
47	1	5.492	24.23	382.68

	2	5.492	32.20	508.51
48	1	5.584	1.42	22.43
	2	5.584	1.08	17.06
49	1	5.559	2.49	39.37
	2	5.559	2.45	38.64
50	1	5.717	13.10	206.86
	2	5.717	12.30	194.23
51	1	5.726	21.80	344.24
	2	5.726	26.70	421.62
	3	5.726	24.20	382.14
	4	5.726	32.50	513.21
	5	5.726	28.40	448.46
	6	5.726	32.00	505.31
	7	5.726	31.20	492.68
	8	5.726	31.90	503.73
52	1	5.79	22.86	361.05
	2	5.79	25.25	398.78
53	1	5.952	12.80	202.12
54	1	5.954	17.92	282.97
55	1	5.992	20.90	330.03
	2	5.992	32.90	519.52
	3	5.992	24.50	386.88
	4	5.992	23.50	371.09
	5	5.992	28.60	451.62
	6	5.992	27.90	440.57
56	1	6.032	12.75	201.32
57	1	6.154	0.67	10.65
	2	6.154	1.15	18.17
58	1	6.203	21.48	339.15
59	1	6.215	1.86	29.39
	2	6.215	1.84	29.12
60	1	6.596	13.51	213.38
	2	6.596	19.53	308.40
	3	6.596	18.64	294.35
	4	6.596	18.42	290.92
61	1	6.776	15.38	242.79
62	1	6.811	9.60	151.59
	2	6.811	11.03	174.17
63	1	6.858	16.96	267.77
	2	6.858	14.95	236.12

64	1	7.011	9.40	148.43
	2	7.011	12.10	191.07
	3	7.111	12.04	190.16
65	1	7.181	12.31	194.35
	2	7.181	10.64	167.97
66	1	7.208	10.83	171.07
	2	7.208	15.96	252.06
67	1	7.335	0.76	12.01
	2	7.335	1.02	16.09
68	1	7.344	1.05	16.62
	2	7.344	1.26	19.88
69	1	7.431	0.77	12.20
70	1	7.493	8.90	140.54
71	1	8.003	8.40	132.64
	2	8.003	10.70	168.96
72	1	8.261	8.15	128.70
	2	8.261	8.30	131.06
73	1	8.442	0.71	11.14
	2	8.442	0.73	11.45
74	1	8.609	8.60	135.88
	2	8.609	13.18	208.05
	3	8.609	8.95	141.28
75	1	9.178	5.99	94.63
	2	9.178	9.87	155.80
76	1	9.512	0.31	4.89
	2	9.512	0.47	7.44
77	1	9.929	2.20	34.80
	2	9.929	1.97	31.18

(b) Sample 5

Position	Bead	Y Position (mm)	Velocity ($\mu\text{m}/\text{sec}$)	Force (pN)
1	1	1.925	182.56	2882.80
	2	1.925	181.70	2869.22
2	1	2.362	206.20	3256.09
3	1	2.929	179.70	2837.63
	2	2.929	121.60	1920.18
4	1	3.08	96.50	1523.83
	2	3.08	99.30	1568.04
5	1	3.137	103.96	1641.63

	2	3.137	160.10	2528.13
6	1	3.163	164.40	2596.03
7	1	3.289	104.35	1647.76
	2	3.289	75.28	1188.79
	3	3.289	139.32	2200.07
8	1	3.574	128.50	2029.14
	2	3.574	134.15	2118.36
9	1	3.724	77.99	1231.52
	2	3.724	99.10	1564.83
10	1	4.067	53.64	846.99
11	1	4.293	65.71	1037.59
12	1	4.65	39.75	627.65
	2	4.65	50.76	801.61
13	1	4.707	40.11	633.44
14	1	4.739	53.49	844.71
15	1	5.058	65.60	1035.90
	2	5.058	53.79	849.33
16	1	5.383	20.15	318.20
	2	5.383	33.48	528.75
17	1	5.485	31.51	497.56
	2	5.485	34.11	538.64
18	1	5.543	30.97	489.11
19	1	5.686	17.17	271.13
	2	5.686	28.45	449.23
20	1	5.77	24.60	388.45
	2	5.77	24.66	389.39
21	1	5.952	22.12	349.22
	2	5.952	24.40	385.38
22	1	6.163	21.79	344.14
23	1	6.372	16.60	262.13
	2	6.372	16.20	255.81
24	1	6.533	11.34	179.07
	2	6.533	17.00	268.45
25	1	6.6	14.13	223.13
	2	6.6	11.35	179.23
26	1	6.696	17.77	280.59
27	1	6.754	8.75	138.19
28	1	6.793	19.90	314.24
	2	6.793	22.50	355.30
	3	6.793	22.30	352.14

29	1	6.967	11.10	175.28
30	1	6.983	14.34	226.44
	2	6.983	14.08	222.36
	3	6.983	15.16	239.40
31	1	6.945	8.13	128.45
32	1	7.165	11.44	180.65
33	1	7.231	14.90	235.27
	2	7.231	10.26	161.99
34	1	7.27	13.61	214.91
35	1	7.344	11.40	180.02
	2	7.344	8.39	132.49
36	1	7.428	9.51	150.17
37	1	7.648	7.62	120.34
	2	7.648	10.69	168.87
38	1	7.679	10.36	163.59
39	1	7.759	12.37	195.33
40	1	7.847	6.25	98.69
	2	7.847	9.66	152.54
	3	7.847	9.52	150.33
41	1	7.799	10.33	163.12
42	1	7.904	7.29	115.12
	2	7.904	9.50	150.01
43	1	7.935	9.37	147.96
44	1	7.998	10.55	166.59
45	1	8.103	9.52	150.33
	2	8.103	14.20	224.23
	3	8.103	9.20	145.28
46	1	8.128	10.46	165.13
47	1	8.289	7.90	124.75
48	1	8.322	7.93	125.21
	2	8.322	12.02	189.85
49	1	8.438	7.34	115.87
50	1	8.578	7.50	118.43
	2	8.578	4.97	78.48
51	1	8.636	6.82	107.74
	2	8.636	10.86	171.54
52	1	9.004	6.46	102.01
	2	9.004	7.45	117.64
	3	9.004	8.10	127.91
	4	9.004	10.74	169.59

53	1	9.121	4.92	77.62
54	1	9.375	7.14	112.75
	2	9.375	6.32	99.80
	3	9.375	4.85	76.59
	4	9.375	7.30	115.27
55	1	9.531	4.62	72.95
	2	9.531	5.63	88.90
56	1	9.609	4.20	66.32
	2	9.609	5.20	82.11
57	1	9.71	4.03	63.56
58	1	9.719	4.95	78.21
59	1	9.939	3.66	57.86
60	1	9.97	4.14	65.37
61	1	10.062	4.45	70.25
62	1	10.756	2.64	41.64
	2	10.756	3.02	47.76
63	1	11.495	2.60	41.06
64	1	11.506	2.62	41.37
65	1	12.503	2.40	37.90

All of the force data taken from each of the five samples was then combined into one complete plot of force versus position, shown in Figure 18, to characterize the bar magnet used in experimentation.

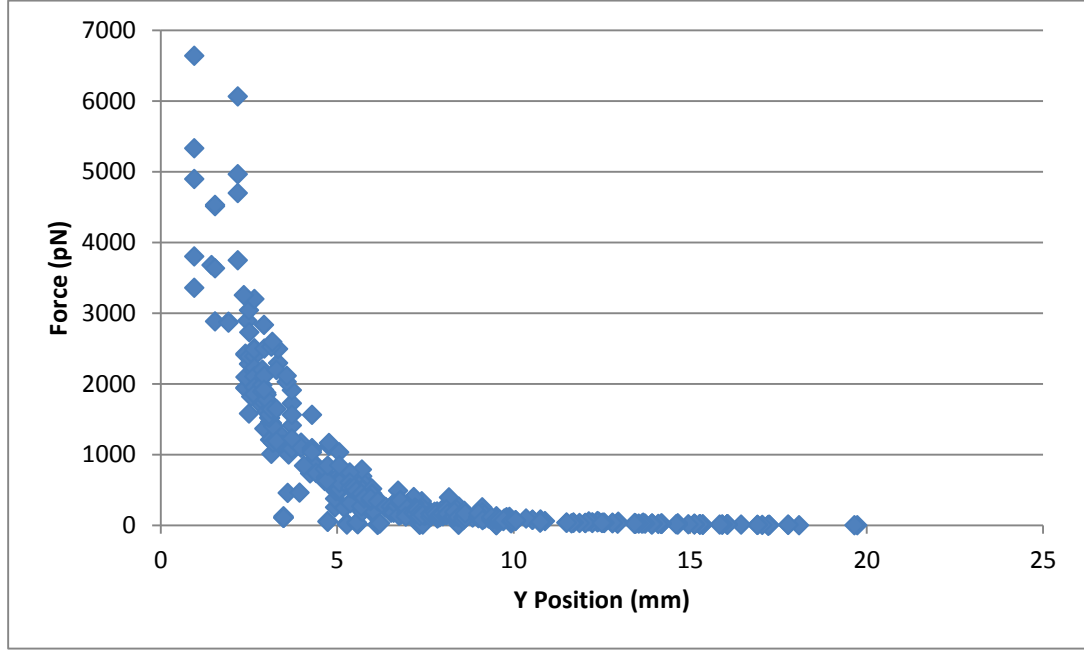


Figure 18: Force Distribution of Bar Magnet. Plot of force at various positions within working range of system for all data acquired during experimentation.

Fitting Data to Theoretical Model Equation

Now that an experimental curve of force as a function of position had been generated, the next step was to fit this experimental data to a theoretical equation, Equation 7, of the same curve shape. For a rectangular bar magnet, the strength of the magnetic field on its central axis can be quantified as a function of distance x from the magnet by the formula below; C is the maximum magnetic field strength of the magnet, W , L , and T are the width, length, and thickness of the magnet respectively, B_r is the magnetic field strength at a point on the surface of the magnet, and B is the magnetic field strength at distance x . Inputting the W , L , T , and B_r values of 0.25 in, 0.25 in, 1 in, and 1.45 T, respectively, into Equation 7 and plotting the magnetic field strength as a function of distance, Figure 19 is obtained.

$$B = \frac{B_r}{\pi} \left[\tan^{-1} \left(\frac{W*L}{2x\sqrt{4x^2+W^2+L^2}} \right) - \tan^{-1} \left(\frac{W*L}{2(x+T)\sqrt{4(x+T)^2+W^2+L^2}} \right) \right] \quad (\text{Equation 7})$$

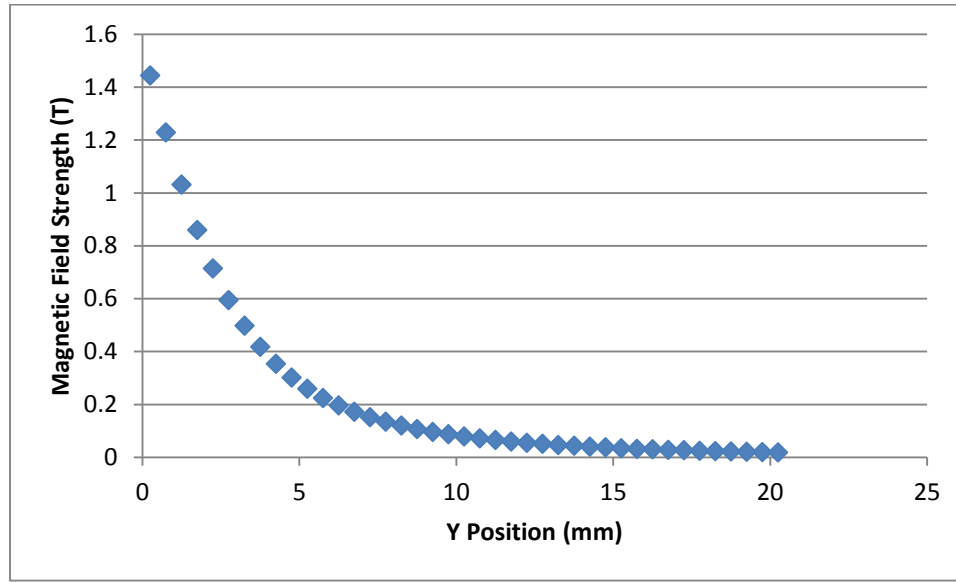


Figure 19: Theoretical magnetic field strength decay of a bar magnet with dimensions of 0.25 in x 0.25 in x 1 in as distance away from the magnet increases.

Although the theoretical curve is not one of force values, it can still be clearly seen that the theoretical distribution of magnetic field strength over distance follows the same shape of curve as the experimental distribution of magnetic force over distance. An easy way to accurately convert magnetic field strength to physical forces acting on spherical particles does not exist. However, the base function of Equation 7 that provides the shape of the curve can still be scaled to fit the experimental data obtained. Using the curve-fitting software, Graphpad Prism, and inputting Equation 7 as the model equation, Equation 8 was outputted as the ideal equation to fit the experimental data. Note that for the bar magnet used in this system, the W , L , and T dimensions are 0.25 in, 0.25 in, and 1 in respectively. Equation 8 was then plotted against the experimental data in Figure 20.

$$\text{Theoretical Force} = 3251 * \left[\tan^{-1} \left(\frac{W*L}{2x\sqrt{4x^2+W^2+L^2}} \right) - \tan^{-1} \left(\frac{W*L}{2(x+T)\sqrt{4(x+T)^2+W^2+L^2}} \right) \right]$$

(Equation 8)

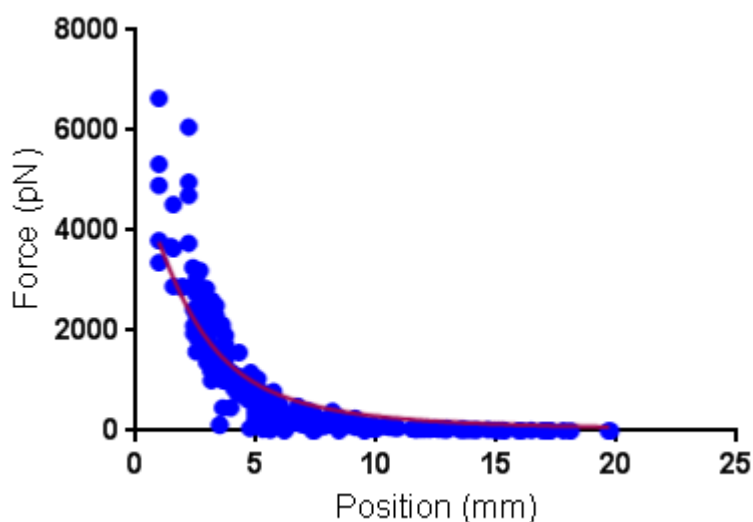


Figure 20: Experimental force data overlaid by the theoretical curve outputted by the curve-fitting software.

By using a base function that matches the shape of the experimental data along with curve-fitting software to scale the equation by the appropriate coefficient to fit the magnitude of the experimental data, an empirical function describing the relationship between force and distance for the specific bar magnet used during experimentation was developed.

Deformation of Beads in Bovine Thrombi

Three bovine thrombi samples, all coming from the same blood bag, were tested; of interest was to observe the nature of the displacement responses of the beads, the magnitude of the displacement, and whether there was consistency in response and magnitude among samples. When testing each sample, data was collected at 10 positions within the working range of the system. The majority of the beads showed consistent responses in all three samples in regards to the response shape, shown in Figure 21. A moving average curve was also plotted to smooth out

irregular peaks and valleys to better visualize the displacement response; the moving average is the average of the previous two data points and the current data point.

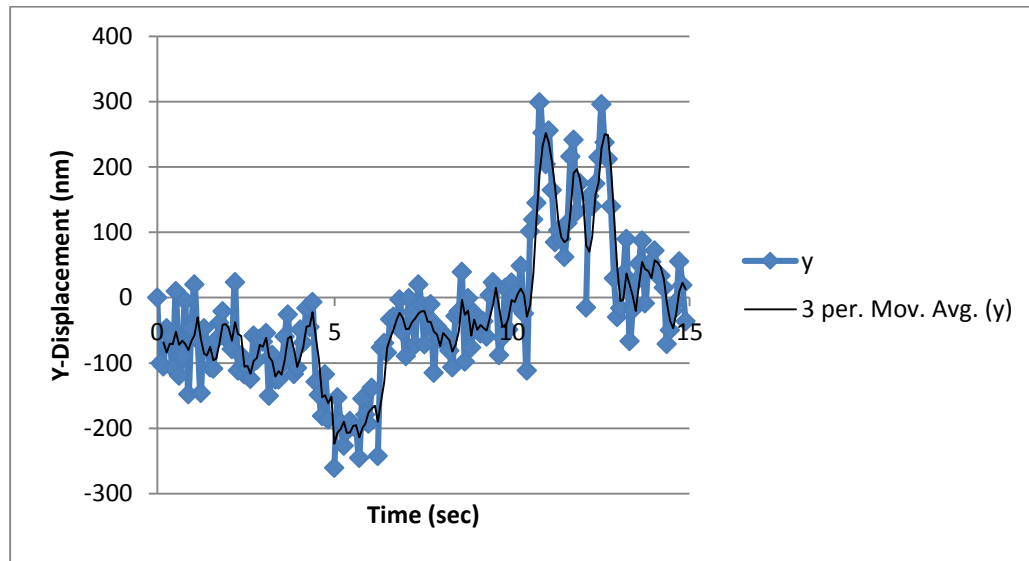


Figure 21: Common Displacement Response Shape in Bovine Thrombus. Displacement of a bead within a bovine thrombus sample. This response shape was consistently observed among trials conducted on thrombi.

Examining the displacement of the bead across the timespan of the trial, the following conclusions were drawn:

- During the first three seconds when the beads were imaged without the magnet in the system to determine the baseline displacement error, the minimal displacement on the order of 100 nm is likely noise and thermal motion of the beads.
- During the fourth and fifth seconds when the magnet was slid into the system and the beads were exposed to the magnetic force, there was a clear response of the beads as the displacement steps fairly immediately towards the magnet.
- Around the seventh second, the displacement steps back towards its baseline position. This occurs even though the magnet was still in the system at this time.

- At around the tenth second when the magnet was removed from the system and the beads were no longer exposed to a force, the displacement actually steps the opposite way in response. This opposite step response was roughly equal in magnitude to the first displacement step occurring around the fourth second of the trial.
- The beads began to drift back towards their baseline position for the remainder of the trial.

Next, it was desired to determine whether the force to deformation ratio, a local spring constant, was consistent across the positions tested in the uniform blood clot. At each position, three runs were conducted. The defined displacement for a trial was calculated by taking the average value of the displacement step observed between four and six seconds and subtracting from that the average value of the baseline position between one and three seconds. The displacements for the three runs were then averaged together to determine the displacement at the bead's position. The force at the bead's position was calculated using Equation 8. Table 6 shows the force value, displacement average, and spring constant value for each bead position tested, and the standard deviation of the measured displacement average.

Table 6: Summary of data for three bovine thrombi tested.

a) Sample 1

Position	Bead	Y (nm)	Force (pN)	Displacement Average of 3 runs (nm)	Displacement Standard Deviation of 3 runs (nm)	Spring Constant k (pN/nm)
1	1	0.86	3850.84	133.89	33.58	28.76
	2	1.02	3645.90	97.42	20.75	37.42
2	1	3.29	1596.41	231.34	37.04	6.90
	2	3.25	1620.27	207.26	20.54	7.82
3	1	4.64	1020.56	159.41	74.59	6.40
	2	4.63	1021.19	196.43	58.43	5.20
	3	4.78	976.27	185.85	62.84	5.25
4	1	6.69	569.37	131.63	26.27	4.33
	2	6.37	618.64	187.75	18.39	3.29
5	1	8.23	393.80	210.90	74.83	1.87
	2	8.36	382.04	180.83	52.88	2.11
6	1	11.21	217.30	190.23	40.02	1.14
7	1	12.68	169.36	156.71	24.03	1.08
	2	12.64	170.54	151.26	29.82	1.13
	3	12.79	166.62	147.68	21.39	1.13
8	1	7.75	439.80	197.81	34.62	2.22
	2	7.60	454.78	210.74	53.95	2.16
9	1	6.63	578.86	147.51	48.87	3.92
	2	6.42	610.46	164.49	57.66	3.71
10	1	4.10	1212.41	212.76	8.76	5.70

b) Sample 2

Position	Bead	Y (nm)	Force (pN)	Displacement Average of 3 runs (nm)	Displacement Standard Deviation of 3 runs (nm)	Spring Constant k (pN/nm)
1	1	2.26	2317.21	268.49	28.17	8.63
2	1	4.27	1148.00	244.57	43.96	4.69
	2	4.43	1088.13	254.51	52.40	4.28
	3	4.61	1028.22	241.62	35.58	4.26
3	1	5.63	758.15	160.82	76.82	4.71
	2	5.49	790.01	224.16	79.49	3.52
4	1	7.57	458.62	211.00	38.30	2.17
	2	7.87	426.95	181.11	22.85	2.36
5	1	9.00	332.95	207.53	85.73	1.60
	2	8.72	353.63	210.87	75.62	1.68
6	1	10.37	253.78	288.30	32.81	0.88
	2	10.23	260.64	305.87	101.50	0.85
	3	10.10	267.08	343.49	82.91	0.78
7	1	11.79	196.37	238.99	50.58	0.82
	2	11.72	198.80	243.67	63.37	0.82
8	1	12.82	165.75	327.80	16.87	0.51
	2	13.00	161.13	304.31	32.94	0.53
9	1	10.87	231.00	368.86	127.82	0.63
	2	10.91	229.23	320.48	122.91	0.72
	3	11.13	220.54	340.14	132.14	0.65
10	1	8.72	353.36	319.55	3.38	1.11
	2	8.70	355.36	282.49	15.25	1.26
	3	9.00	333.09	307.79	15.61	1.08

c) Sample 3

Position	Bead	Y (nm)	Force (pN)	Displacement Average of 3 runs (nm)	Displacement Standard Deviation of 3 runs (nm)	Spring Constant k (pN/nm)
1	1	1.57	2984.99	327.76	16.20	9.11
2	1	2.40	2199.63	278.05	39.43	7.91
	2	2.57	2071.36	232.09	37.03	8.92
3	1	4.17	1186.07	224.53	40.50	5.28
4	1	5.56	773.84	139.57	35.61	5.54
	2	5.46	796.01	160.63	45.19	4.96
	3	5.26	843.31	219.28	39.55	3.85
5	1	6.65	575.65	251.38	35.85	2.29
	2	6.72	565.31	238.54	55.76	2.37
6	1	7.48	468.59	212.97	18.87	2.20
	2	7.55	460.70	149.60	33.98	3.08
	3	7.29	489.60	214.83	18.23	2.28
7	1	8.87	342.13	192.95	52.27	1.77
	2	9.14	323.76	188.03	31.68	1.72
	3	10.51	246.99	161.09	29.97	1.53
8	1	10.41	251.85	170.50	12.18	1.48
9	1	11.44	208.62	296.98	56.33	0.70
	2	11.46	207.89	290.90	61.13	0.71
10	1	6.67	572.36	220.93	24.79	2.59
	2	6.74	561.99	169.87	45.86	3.31

The local spring constant values for all three samples were then plotted together against the position in Figure 22.

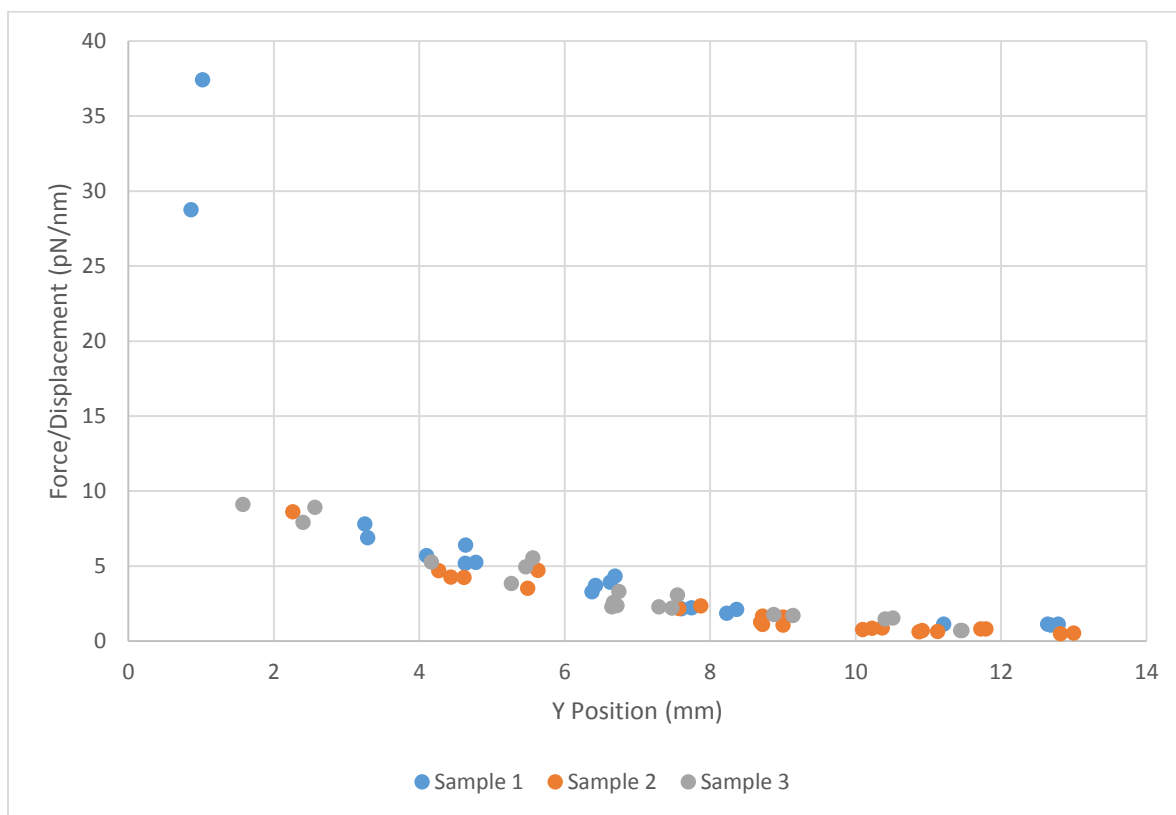


Figure 22: Spring Constant vs Position in Blood Clot. Local spring constant values for three bovine thrombi. Neglecting the two outliers, there is a slight linear decrease in k value as the position increases.

Bovine blood was centrifuged to extract the platelet-rich plasma with buffy coat and the packed red blood cells, which were each tested and compared with the whole blood coming from the same bag. A summary comparison of responses of each of the three samples is shown in Figure 23.

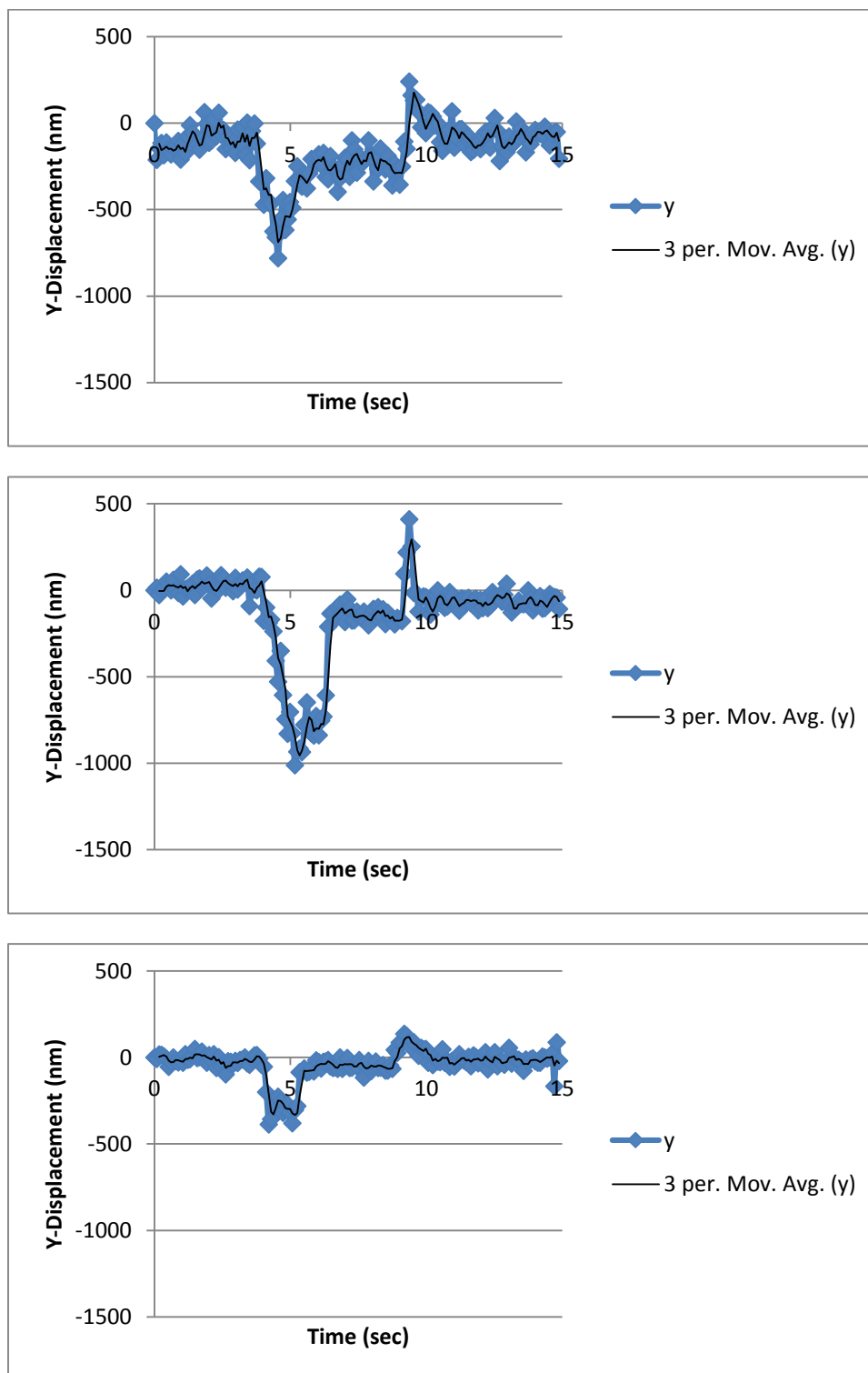


Figure 23: Characteristic bead displacement responses in three different mediums: Top plot (Whole Bovine Blood), middle plot (Platelet-Rich Plasma and White Buffy Coat Solution), and bottom plot (Packed Red Blood Cells).

The displacement response shape was very similar across all three types of medium. The peak displacement of the beads was greater in the platelet-rich plasma sample than in the whole blood sample, while the displacement of the beads in the packed red blood cells sample was less. In Figure 24, each of the three samples was then imaged with bright-field microscopy to observe how tightly the cells and constituents were packed together.

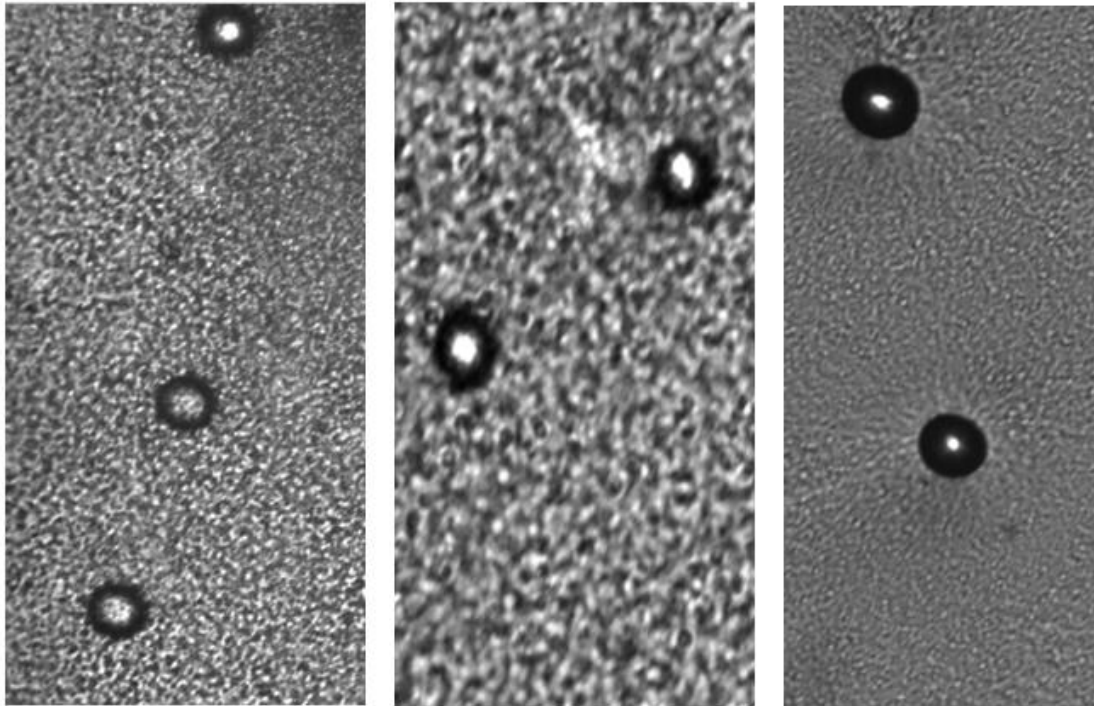


Figure 24: Bright-field Microscopy of each sample from left to right: Packed Red Blood Cells, Whole Blood, and Platelet-Rich Plasma and White Buffy Coat Solution.

It is clearly visible that the constituents of the platelet-rich plasma and white buffy coat samples are most loosely compacted, while the cells in the packed red blood cells sample are much more tightly compacted than the other two samples.

Chapter 4

Discussion

The objective of the project was to develop a method of studying thrombus rheology on a local level using a magnetic bead microrheometry system. The key to achieving a useful system that can calculate local elasticities at various points in a heterogeneous thrombus is to have a method of measuring the stresses and strains at each location. By measuring the displacement of magnetic beads through the sample with particle tracking software, the strain at a given position can be obtained. From empirically deriving an equation of magnetic force as a function of distance away from the magnet based on experimental data taken using glycerol-albumin solutions of known viscosity, stress measurements can also be obtained. The effectiveness of these steps are analyzed to determine the utility of this developed system.

Polyacrylamide Hydrogel Testing with Electromagnet

The first experiments to calibrate a magnetic bead microrheometry system consisted of a soft iron core electromagnet applying force to paramagnetic beads embedded in polyacrylamide hydrogels. The electromagnet was used first because it could be controlled through a relay mechanism without having to be moved once placed in the system. Polyacrylamide hydrogels were chosen at first to test because the cross-linking mesh network created during the formation of the gel is similar to that of a thrombus. Using Hooke's Law, the elasticity at each position tested within the system could be calculated, so long as the displacement of the magnetic beads were linear elastic in nature. However, during experimentation, no useful data of linear elastic displacement was obtained; bead responses consisted of only noise and random drift. Thus, the electromagnet and hydrogels both presented issues that prevented calibration of the system. Electromagnets can potentially leave a residual magnetic field after current flow has stopped; any

residual forces left on the magnetic beads could introduce enough noise to distort the displacement response because the magnitude of displacement is only on the nanometer scale. Degaussing an electromagnet involves running an alternating current through the magnet to decrease the magnitude of the remnant field. If in the future, further experimentation with the electromagnet is warranted, adding an AC current pulse immediately after the Labview controlled DC current pulse would be an improvement. Due to the large amount of drift exhibited by beads in trials with the electromagnet on polyacrylamide hydrogels, it appeared that the beads were not well-adhered to the matrix. Increasing the effective Modulus of Elasticity of the gel to increase the cross-linking would increase the resistance to bead motion, and thus potentially stop bead drift. However, since the beads were already displacing less than five percent of the bead diameter, decreasing bead displacement even further by increasing the stiffness of the gel would make it very difficult to discern actual experimental responses from simply random thermal motion.

Viscous Fluid Testing with Bar Magnet

The next type of experimental setup featured a changed sample material and mode of force application; the samples now consisted of varied concentrations of glycerol-albumin solutions, with the electromagnet being exchanged for a neodymium bar magnet. By tracking the motion of beads in fluid rather than a gel, much greater displacements were observed that certainly could not be attributed to simply noise or drift. This instilled confidence that the beads were responding to a controlled, externally applied force. In order to calculate force values from the Stoke's drag force equation, the velocity of bead motion was needed; this was calculated by dividing the tracked displacement of the beads by the duration of magnet application. Three different samples of equal viscosity were tested to verify that the same values of velocity at each

position was consistent from one sample to the next. After combining the velocity data from over sixty sample positions taken over the three samples of equal velocity, the velocity distribution of each sample aligned very well (Figure 17). This data validated the new experimental methodology, because the large sample size coupled with the consistent velocity distributions indicated repeatable performance from the bar magnet and repeatable response from the beads.

Force Calculations and Empirically Derived Equation

After experimentally obtaining velocity data of beads at various positions in the system, the Stoke's drag force equation was used to determine the force induced from the bar magnet at each position tested. The force values calculated had an order of magnitude in the piconewtons range, which was expected based off of previous microrheometry work.²¹ To verify that the force values calculated for the bar magnet were repeatable, and to increase the amount of force data collected before deriving an empirical equation, two new glycerol-albumin solutions were tested. These new samples were of different viscosities from the original three samples; though the velocities of beads moving through the new samples would be different, the final force values calculated should still match that of the old samples at corresponding positions. After tracking the beads, calculating the velocity of the beads, and using the Stoke's equation to yield force values, it was seen clearly that this was indeed the case. By taking multiple measures to ensure the data obtained was repeatable by testing samples of equal viscosity to ensure the velocities of the beads were the same, then testing samples of different viscosities to ensure that the calculated forces were the same, and additionally verifying that the magnitude of the calculated forces matched previous literature, there was enough assurance in the data to proceed. A curve-fitting software was then used to take the raw data of force distribution and output a final equation expressing the bar magnet force as a function of distance away from the magnet. Because of the many steps

undertaken during experimentation to ensure that the data was repeatable, there is confidence that this empirically derived equation is an accurate model of the bar magnet's force distribution. However, there are some limitations to this equation that must be noted. Firstly, this equation can only be applied to calculate forces at positions that lie within the width of the magnet (.25"), because testing during experimentation was limited to positions with x-coordinates that rested within the width of the bar magnet, thus allowing for the approximation that all displacement was in the y-direction. Also, this equation assumes that the flow of bead motion, which are moving as a result of the drag force induced by the bar magnet, obey all of the assumptions of the Stoke's drag force equation aside from the assumption of a continuous medium, which was corrected for through the Faxen's Law coefficient. As long as these conditions are met, this empirically derived equation can be used when testing other materials to determine local elasticity values.

Experimentation on Bovine Blood Thrombi

Initial results from experimentation with bovine blood thrombi yielded a single response shape that was consistent across virtually all trials conducted (Figure 21). The bead would displace towards the magnet when the magnet was placed into the system, but would immediately step back towards its baseline position within a second. When the magnet was removed, the bead would displace in the opposite direction as previously. The beads are paramagnetic, with the dipoles always aligning with the direction of the magnetic field. Thus, it is unclear as to why any movement of the magnet would cause the bead to displace in the opposite direction. The magnitude of the first displacement step and the second displacement step were roughly equal for most trials conducted, suggesting that the beads are well-adhered to the cross-linked network because the local resistance would be approximately the same moving in any direction.

Additionally, when testing a bead three consecutive times and averaging the measured displacement of the three runs together to produce an average displacement for that position, the standard deviation was greater than what would ideally be desired; the standard deviation ranged from around ten percent to twenty percent of the average displacement for the corresponding position. This variability in displacement measurements causes issues when attempting to calculate a spring constant value. The spring constant values calculated decreased as the position increased. As the position away from the magnet increases, the force at the position decreases; however, because the amount of deformation did not in turn decrease proportionally, the force to displacement ratio did not remain constant across the positions. This means that either the thrombi formed were not uniform, as was originally thought, or that the system is not robust enough to provide the necessary accuracy in measurements that would contribute to more confident spring constant values. The current experimental setup uses a 10X objective lens that when viewed with the high-speed camera, has a resolution of 641.97 nm/pixel. Because the tracking software can track displacements of up to a tenth of a pixel, the error in measurement is around 64 nm. The variability in measurement of 64 nm, when the average displacement of most positions is in the range of 150 nm to 300 nm, is very high.

Without a clear elastic displacement response, and without fully understanding the reason for the response pattern observed, Hooke's Law cannot be used to calculate local elasticity values. Blood clots have been studied in the past for potential viscoelastic properties that develop during the course of fibrin polymerization and cross-linking from the liquid to solid transition.³⁰ However, the initial movement of the bead when it steps towards the magnet and then back towards the baseline position cannot even be considered viscoelastic, as the direction is away from the magnet and not linearly time-dependent. It was not initially considered that the constituents of blood such as platelets, red blood cells, or other components would impact the deformation being studied, but the results indicate that this assumption may be flawed. Testing of

thrombi samples after separating constituents such as platelets and red blood cells again showed the same response shape, so the effects of these constituents could not be determined. However, the magnitude of the displacement in the packed red blood cell samples was less than in whole blood thrombi, and greater in platelet-rich plasma thrombi. Examining these samples with bright-field microscopy explained the difference in magnitude observed. The constituents of the platelet-rich plasma and white buffy coat samples are most loosely packed, while the cells in the packed red blood cells sample are much more tightly packed than the other two samples. Thus, beads moving through packed red blood cells would experience greater resistance than beads moving through the platelet-rich plasma and white buffy coat solution, leading to the much smaller displacement. Though the difference in displacements among the three samples was explained, there is still no justification for the cause of the strange response shape in these samples.

Another factor not considered in these preliminary experiments is the susceptibility of red blood cells to an external magnetic field. Human erythrocytes contain a high concentration of hemoglobin; chemical bonds between an iron atom and the rest of the heme group exist within the hemoglobin protein molecule. Results of past work on erythrocytes revealed that the presence of iron in the cells lead to magnetophoretic mobility. Additionally, deoxygenated erythrocytes exhibit a significant diamagnetic component, while oxygenated erythrocytes exhibit a paramagnetic component relative to the suspension medium.³¹ Thus, the impact of this phenomenon on this project, in terms of tracking magnetic bead displacement, should be explored by conducting a control experiment, where non-magnetic beads are embedded within a thrombus sample. Because these non-magnetic beads should not respond to an external magnetic field, if any displacement of the beads do occur, it would have to be associated with mobility of the red blood cells causing the beads to move in turn.

Conclusions and Future Work

The objective of the project was to develop a method of studying thrombus rheology on a local level using a magnetic bead microrheometry system. Using a microscope and high-speed camera to image a system where a bar magnet applies a force to paramagnetic beads embedded in a material, the beads can then be tracked over time to determine the resulting deformation.

Viscous glycerol-albumin solutions with viscosities ranging from 2.1 cP to 12 cP were used to calibrate the system. Obtaining velocity data from the tracked displacement plots and using Stoke's law to calculate drag forces, a distribution of forces throughout the system was obtained. An equation was fit to the experimental data to create an empirical expression for the force within the working range of the system as a function of the bead position. With the forces in the system now known, materials of unknown elasticity could now be tested. Results of experiments on bovine thrombi showed initial elastic displacement responses, but other subsequent behaviors coupled with drift made the responses more difficult to characterize. Testing deformation in different constituents of bovine blood such as platelet-rich plasma and packed red blood cells did not show significantly different response patterns. This project has developed and put a system in place to acquire and analyze data of microrheology experiments on unknown materials. Future work must focus on studying the consistent, yet unintuitive, response patterns being observed. From there, thrombi of unknown elasticity formed in conditions closely resembling those *in vivo* can be studied.

There are many improvements and methods that can be undertaken to further the work already completed. Firstly, steps to bolster the robustness of the system should be taken such as increasing the magnification of the objective lens or using a particle tracker with a greater pixel resolution in order to track displacements with a smaller amount of error than 64 nm. Additionally, the magnetic field must also be mapped out for a greater area of the working range of the system, so that positions can be studied even if they are not around the center of the

magnet. Another area of exploration is testing bovine thrombi with the electromagnet; the benefit of the electromagnet is in its ability to deliver a force instantaneously to limit the viscoelastic, time-dependent component of the displacement response. The electromagnet did not yield viable results when testing polyacrylamide hydrogels, but it was unclear as to whether the issue rested with the method of creating the hydrogel samples or with the electromagnet itself. Testing blood samples with the electromagnet and comparing the response shapes with the results from the bar magnet would be valuable in studying the effects and errors of manually having to place the bar magnet into and out of the system. Lastly, the preliminary results of testing bovine blood must be studied in depth to address the issues discussed in the displacement response pattern. When the reasons and mechanisms causing this response pattern are understood, Hooke's law or another appropriate model can be applied to calculate localized elasticity values of thrombi.

BIBLIOGRAPHY

1. Mensah G a, Brown DW. An overview of cardiovascular disease burden in the United States. *Health Aff (Millwood)*. 2007;26(1):38-48. doi:10.1377/hlthaff.26.1.38.
2. Lloyd-Jones D, Adams RJ, Brown TM, et al. Heart disease and stroke statistics--2010 update: a report from the American Heart Association. *Circulation*. 2010;121(7):e46-e215. doi:10.1161/CIRCULATIONAHA.109.192667.
3. Chandran KB, Rittgers SE, Yoganathan AP. *Biofluid Mechanics: The Human Circulation*. 2nd ed. Boca Raton: CRC Press; 2012:451.
4. Lusis AJ. Atherosclerosis. *Macmillan Mag Ltd*. 2000;407(September):233-242.
5. Wootton DM, Ku DN. Fluid mechanics of vascular systems, diseases, and thrombosis. *Annu Rev Biomed Eng*. 1999;1:299-329. doi:10.1146/annurev.bioeng.1.1.299.
6. Taura LS, Ishiyaku IB, Kawo AH. The use of a continuity equation of fluid mechanics to reduce the abnormality of the cardiovascular system: A control mechanics of the human heart. *J Biophys Struct Biol*. 2012;4(1):1-12. doi:10.5897/JBSB11.010.
7. Rabby MG, Shupti SP, Molla M. Pulsatile Non-Newtonian Laminar Blood Flows through Arterial Double Stenoses. *J Fluids*. 2014;2014:1-14.
8. Groups FH, Facilities SM. *White Paper : Common Complications Associated with Left Ventricular Assist Device (LVAD) Implantation Common Complications with LVAD Implantation Indications for LVAD Implantation*. Portland, OR; :1-7.
9. Eckman PM, John R. Bleeding and thrombosis in patients with continuous-flow ventricular assist devices. *Circulation*. 2012;125(24):3038-3047. doi:10.1161/CIRCULATIONAHA.111.040246.
10. Spronk HM, van der Voort D, Ten Cate H. Blood coagulation and the risk of atherothrombosis: a complex relationship. *Thromb J*. 2004;2(1):12. doi:10.1186/1477-9560-2-12.
11. Adams RLC, Bird RJ. Review article: Coagulation cascade and therapeutics update: relevance to nephrology. Part 1: Overview of coagulation, thrombophilias and history of anticoagulants. *Nephrology (Carlton)*. 2009;14(5):462-470. doi:10.1111/j.1440-1797.2009.01128.x.
12. Green D. Coagulation cascade. *Hemodial Int*. 2006;10 Suppl 2:S2-S4. doi:10.1111/j.1542-4758.2006.00119.x.

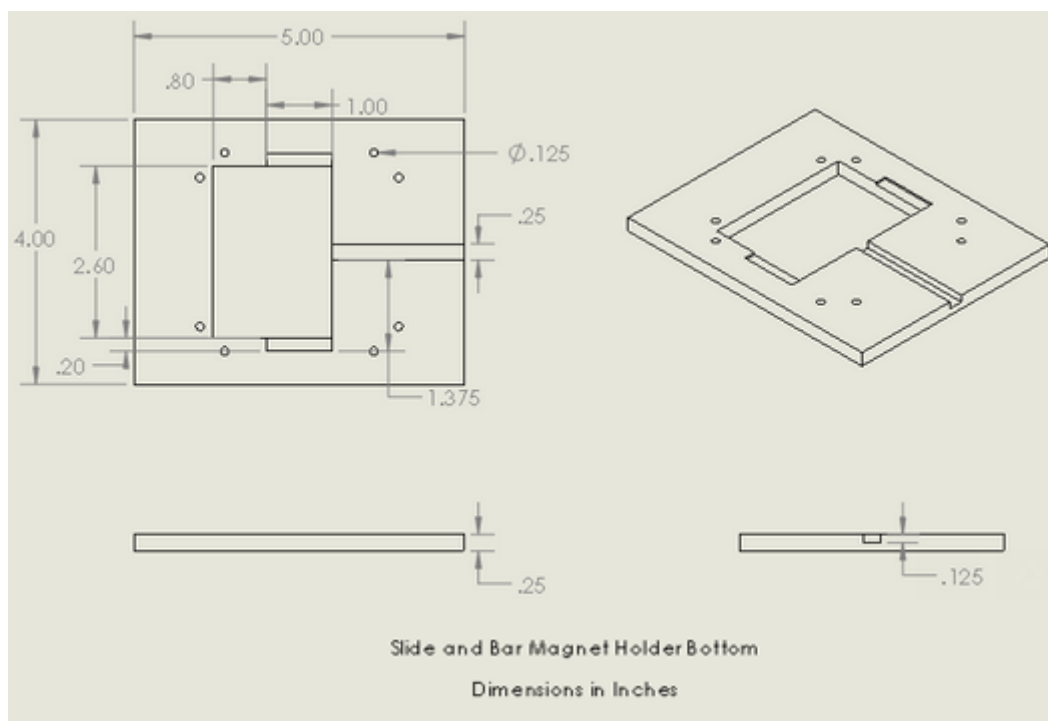
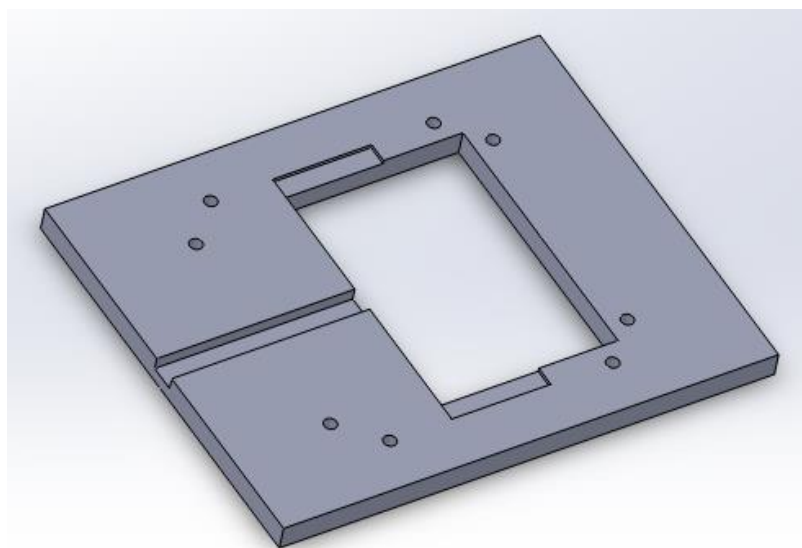
13. Schattner MA, Lazzari MA. *Platelet Release Reaction in Whole Blood*. Buenos Aires; 1983:759-763.
14. Gailani D, Renné T. The intrinsic pathway of coagulation: a target for treating thromboembolic disease? *J Thromb Haemost*. 2007;5(6):1106-1112. doi:10.1111/j.1538-7836.2007.02446.x.
15. Genest J, Gotto AM, Kastelein JJP, et al. A Randomized Trial of Rosuvastatin in the Prevention of Venous Thromboembolism. *N Engl J Med*. 2009;360:1851-1861.
16. Gardel ML, Valentine MT, Weitz DA. *1 Microrheology*. Cambridge; 1999:1-55.
17. Ryan E a, Mockros LF, Weisel JW, Lorand L. Structural origins of fibrin clot rheology. *Biophys J*. 1999;77(5):2813-2826.
<http://www.pubmedcentral.nih.gov/articlerender.fcgi?artid=1300553&tool=pmcentrez&rendertype=abstract>.
18. Weigandt KM, White N, Chung D, et al. Fibrin clot structure and mechanics associated with specific oxidation of methionine residues in fibrinogen. *Biophys J*. 2012;103(11):2399-2407. doi:10.1016/j.bpj.2012.10.036.
19. Chen Y. Rheological Properties of Fibrin Clots. 2012:12-111.
20. Ziemann F, Rädler J, Sackmann E. Local measurements of viscoelastic moduli of entangled actin networks using an oscillating magnetic bead micro-rheometer. *Biophys J*. 1994;66(6):2210-2216. doi:10.1016/S0006-3495(94)81017-3.
21. Yang Y, Lin J, Meschewski R, Watson E, Valentine MT. Portable magnetic tweezers device enables visualization of the three-dimensional microscale deformation of soft biological materials. *Biotechniques*. 2011;51(1):29-34. doi:10.2144/000113701.
22. Yamada S, Wirtz D, Kuo SC. Mechanics of living cells measured by laser tracking microrheology. *Biophys J*. 2000;78(4):1736-1747. doi:10.1016/S0006-3495(00)76725-7.
23. Journal KR. Hydrogel microrheology near the liquid-solid transition. *Korea-Australia Rheol J*. 2008;20(3):165-173.
24. Gautreau Z, Griffin J, Peterson T, Thongpradit P. *Characterizing Viscoelastic Properties of Polyacrylamide Gels*; 2006:145.
25. Tse JR, Engler AJ. Preparation of hydrogel substrates with tunable mechanical properties. *Curr Protoc Cell Biol*. 2010;Chapter 10(June):Unit 10.16.
doi:10.1002/0471143030.cb1016s47.
26. Velegol D, Lanni F. Cell traction forces on soft biomaterials. I. Microrheology of type I collagen gels. *Biophys J*. 2001;81(3):1786-1792. doi:10.1016/S0006-3495(01)75829-8.

27. Cengel YA, Cimbala JM. *Fluid Mechanics: Fundamentals and Applications*. Boston: McGraw-Hill Higher Education; 2006:617-618.
28. Scha E, Nørrelykke SF, Howard J. Surface Forces and Drag Coefficients of Microspheres near a Plane Surface Measured with Optical Tweezers. *Langmuir*. 2007;287(9):3654-3665.
29. Liang XM, Han SJ, Reems J-A, Gao D, Sniadecki NJ. Platelet retraction force measurements using flexible post force sensors. *Lab Chip*. 2010;10(8):991-998. doi:10.1039/b918719g.
30. Evans PA, Hawkins K, Williams PR. *RHEOMETRY FOR BLOOD COAGULATION STUDIES*.; 2006:255-291.
31. Zborowski M, Ostera GR, Moore LR, Milliron S, Chalmers JJ. Red Blood Cell Magnetophoresis. *Biophys J*. 2003;84(April):2638-2645.

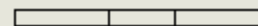
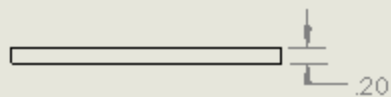
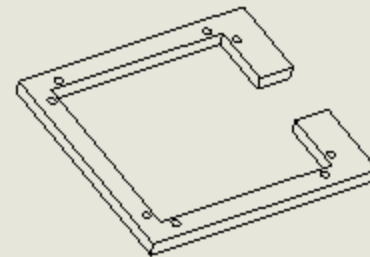
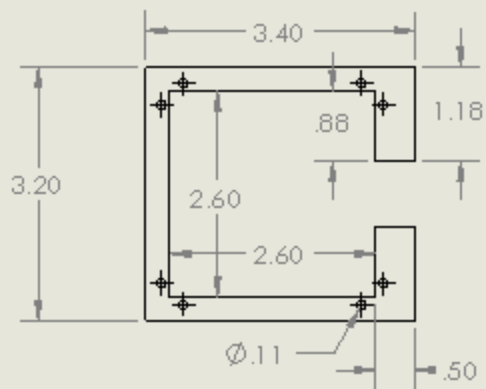
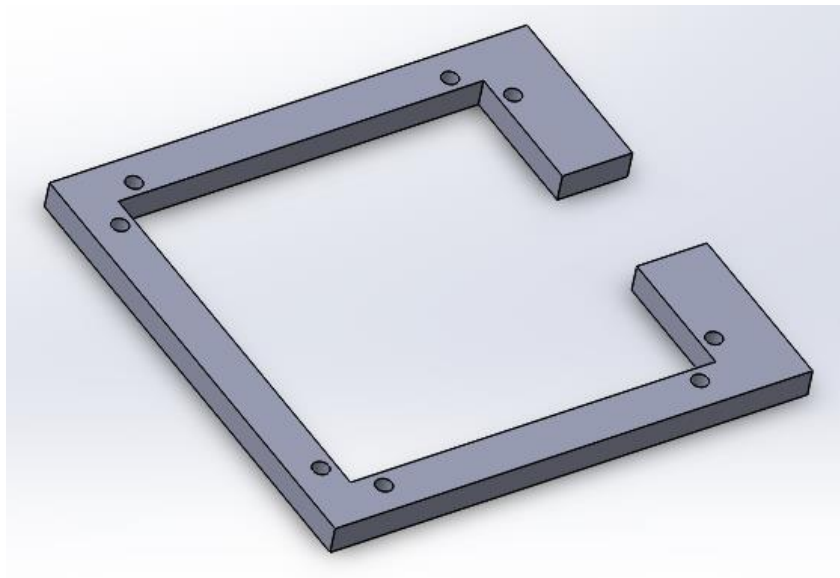
Appendix A

Solidworks Drawing of Sample and Magnet Holder

Part 1: Bottom Component



Part 2: Top Component



Slide and Bar Magnet Holder Top

Dimensions in Inches

ACADEMIC VITA

PRITHVI NILKANT

pzn5025@gmail.com

- EDUCATION** **Bachelor of Science in Mechanical Engineering, Biomedical Engineering (Double Major)**
The Pennsylvania State University - University Park, PA
Schreyer Honors College
Expected Graduation: *May 2015*
Relevant Courses: Thermodynamics, Dynamic Systems, Design Methodology, Manufacturing Processes, Fluid Mechanics, Signals and Systems, Continuum Mechanics, Instrumentation
- WORK EXPERIENCE** **Engineering Leadership Development Program Intern** *May 2014 – August 2014*
Siemens Industry, Inc. - Atlanta, GA
- Investigated effect of pressure due to current interruption on circuit breaker rupture
 - Conducted high interruption current testing, modeled observed ruptures using finite element analysis, and developed strength test used to standardize production of parts
 - Experimental methods using pressure sensor and analysis of data drew interest from others within company wanting to apply system to different projects
 - Established project methodology to help prevent rupture nonconformities that led to estimated losses of **\$190k per year** in the past on one breaker model, can be extended to other models as well
- Research and Development Intern** *May 2013 – August 2013*
Actuated Medical, Inc. - Bellefonte, PA
- Worked on various projects involving innovative actuated technology of medical devices
 - Responsible for early stage performance testing to determine feasibility of projects
 - Developed skills in soldering techniques, working with tissue and bone samples, experiment design, and data analysis
- Undergraduate Researcher** *September 2012 – Present*
Artificial Heart and Cardiovascular Fluid Dynamics Lab - Penn State Biomedical Engineering Department
- Studying localized elasticities and mechanical properties of thrombi to gain insight into thrombus formation and gage risk of embolism
 - Perform thrombus rheology experiments using magnetic bead microrheometry
 - Experience in hydrogel formation, fluorescence microscopy, and particle imaging and tracking
- Counselor** *June 2012 – August 2012*
GreenE Academy Lego Robotics Summer Camp - Pittsburgh, PA
- Supervised upper elementary school children throughout the day
 - Taught basic principles in programming, design, and teamwork
- Host/Cashier** *May 2011 – August 2012*
Eat'n Park Restaurant - Wexford PA

SKILLS SolidWorks Design Software, MATLAB Programming, COMSOL Multiphysics,
Pro/ENGINEER

ACTIVITIES Mentor, Schreyer Honors College Freshman Orientation *Fall 2012*
Hospitality Committee, Penn State IFC/Panhellenic Dance Marathon *2012- Present*

HONORS Tau Beta Pi Engineering Honor Society *Inducted Spring 2014*
Third Place Winner of Penn State Civic Engagement Public Speaking Contest *Fall 2013*

- Sponsored by *The New York Time*, over 1500 student contestants

Louis A. Harding Memorial Scholarship in Mechanical Engineering
Schreyer Honors College Academic Excellence Scholarship
Westinghouse Family Scholarship